Quality Control of $PbWO_4$-Crystals for the $\overline{P}$ANDA Detector

Diplomarbeit
im Fachgebiet Experimentalphysik
Prof. Dr. Volker Metag
II. Physikalisches Institut
Universität Gießen

vorgelegt von

Tobias Eißner
aus Ortenberg

Betreuer: Dr. Rainer Novotny

Contents

Summary

Lead tungstate will be used as scintillation material for the electromagnetic calorimeter of the $\overline{\text{P}}$ANDA detector at the future FAIR facility at Darmstadt. Therefore, the mass production of the tapered lead tungstate crystals was started by the manufacturer BTCP at Bogoroditsk. To guarantee the required physic performances of $\overline{\text{P}}$ANDA, the quality of the crystals has to be verified according to the contract. The crystals have to pass quality test stations installed at CERN and Gießen, respectively. All measured data concerning geometry, longitudinal and transversal transmission, light yield and radiation hardness are collected in a database to maintain the overview and to have fast access to all results.
This thesis documents and has optimized the testing methods of the different facilities and explains the criteria for the individual properties. In particular, several simulations with the so called LITRANI program were performed in order to estimate the systematic and statistical uncertainties of the inspected radiation hardness due to multiple reflected photons and to reconstruct first results of the quality control concerning the light yield. It turns out that the light yield and therefore the light collection efficiency strongly depends on the location of the scintillation process and furthermore on the geometry and the different levels of tapering, respectively. The obtained results confirm the existing non-linearity of the light collection which, however, will not significantly affect the energy response due to the concentration of the main shower deposition within the first third of the crystals for the relevant $\overline{\text{P}}$ANDA energy regime (10 MeV - 10 GeV).
The first two lots which contain 1750 crystals (22% barrel type and 78% forward endcap type) were completely analyzed and show well improved parameters for the quality in comparison to crystals used in previous experiments like CMS. Out of these two lots, 4 crystals had to be rejected due to insufficient light yield and 201 crystals due to the insufficient radiation hardness taking into account the modified and more appropriate specification limit of $\Delta k \leq 1.1\ m^{-1}$. Nevertheless, for the overall results of the quality control it is shown that the expected quality for the mass production was confirmed and remains nearly constant for the next lots.

Chapter 1

Introduction and Motivation

The $\overline{\mathrm{P}}$ANDA[1] detector will be built to perform strong interaction studies especially of antiprotons with nucleons and nuclei. The development comprises a lot of instrumental improvements to cope with the requirements to FAIR[2] like e.g. capability for high intensity, energy and high precision. It will be located as an internal detector at the HESR[3] which is part of the new FAIR facility in Darmstadt (Fig. 1.1).

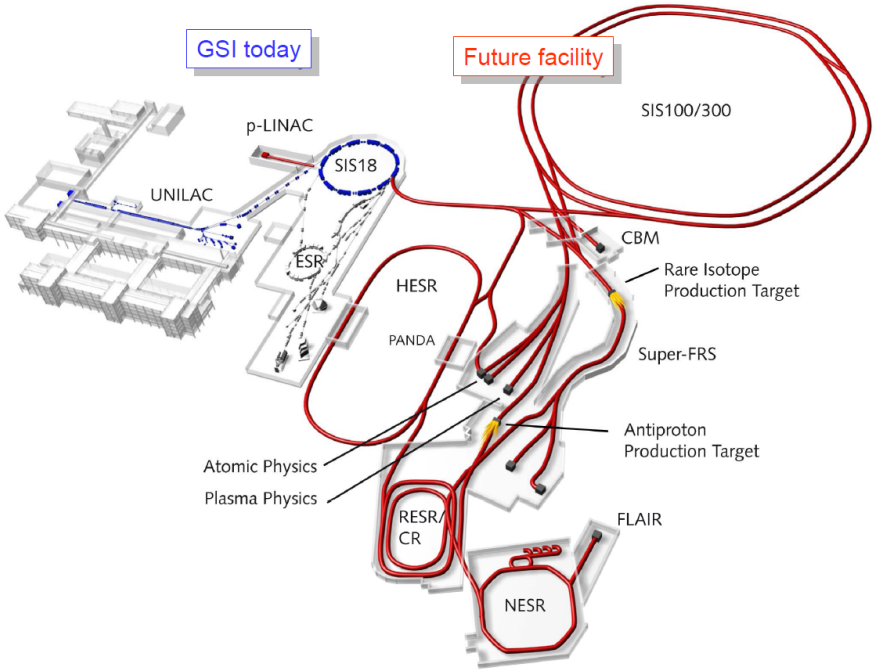

Figure 1.1: Present GSI[4] with the planned FAIR facility [VM].

[1] $\overline{\mathrm{P}}$ANDA = antiProton ANnihilation at DArmstadt
[2] FAIR = Facility for Antiproton and Ion Research
[3] HESR = High Energy Storage Ring
[4] GSI = Gesellschaft für SchwerIonenforschung

The electromagnetic calorimeter (EMC) in the target spectrometer is one of the main components for $\overline{\mathrm{P}}$ANDA. It should provide high energy resolution for photon and meson spectroscopy over a wide range of energy from a few tens of MeV up to several GeV to achieve the physical goals of $\overline{\mathrm{P}}$ANDA. Therefore, the EMC has to fulfill several conditions which will be discussed in this chapter. Also some aspects of the further development of the lead tungstate crystals are introduced in comparison to the ECAL[5]-crystals of the CMS[6] experiment at CERN[7]. A view of the expected $\overline{\mathrm{P}}$ANDA EMC without backward endcap (EC) is illustrated in Fig. 1.2.

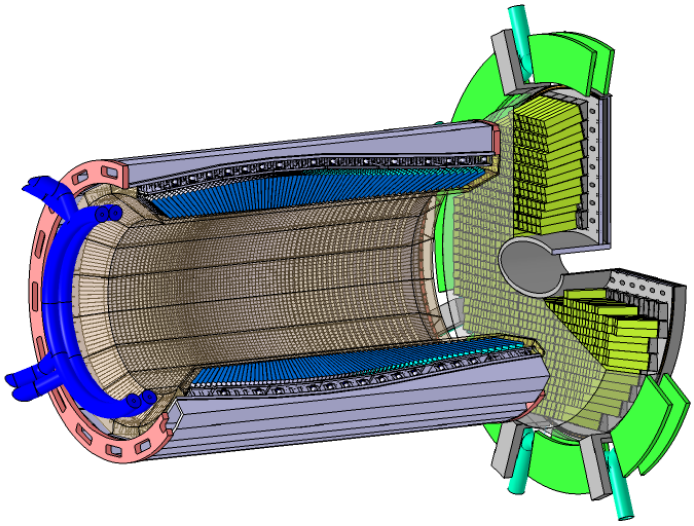

Figure 1.2: A sketch view of the planned $\overline{\mathrm{P}}$ANDA EMC without backward EC [TDR].

1.1 Physics program of $\overline{\mathrm{P}}$ANDA

The $\overline{\mathrm{P}}$ANDA detector offers the opportunity to study the hadron structure and the strong interaction with extraordinary statistics and accuracy. The cooled antiproton beam will be a helpful tool to address questions which extend from the test of fundamental symmetries to the study of Quantum Chromo Dynamics (QCD). QCD is regarded as the basic theory of the fundamental strong interaction and is well understood at short distances below 10^{-15} m. In this regime, with a comparatively small coupling constant ($\alpha_S << 1$), one talks about perturbative QCD. But the experimental knowledge in the non-perturbative ($\alpha_S \leq 1$) regime is rather limited.

[5]ECAL = Electromagnetic CALorimeter
[6]CMS = Compact Muon Solenoid
[7]CERN = Conseil Européen pour la Recherche Nucléaire

The scientific program of $\overline{\mathrm{P}}$ANDA includes several aspects, mostly in the non-perturbative regime, listed below [PPR, VM]:

- Hadron spectroscopy up to the region of charmed mesons and baryons
- Searching for exotic states like glueballs, hybrids and multiquark states
- Study of spin dynamics
- Investigation of hadron properties inside nuclear matter
- Study of the structure of the nucleon
- Study of parton distributions exploiting Drell-Yan production
- Solving open questions concerning CP violation

Spectroscopy has been a prime tool for physics in many levels of structural hierarchy of matter and has played a leading role in the development of quantum mechanics and the standard model. In case of $\overline{\mathrm{P}}$ANDA, spectroscopy experiments for hadron physics are the ideal laboratory to compare the knowledge of QCD with the experimental results. The spectrum of charmonium ($c\bar{c}$) is similar to the one of positronium in case of the electromagnetic interaction. This implies in first approximation a potential $V(r) = a/r + br$ which has to be tested further e.g. for spin dependency. For charmonium, the production via $p\bar{p}$ reactions is advantageous in comparison to e^+e^-. The latter one can only form $J^{PC} = 1^{--}$ states and for all other states the mass resolution is determined by the detector resolution. Other states can only be populated in secondary decays.

$$e^+e^- \rightarrow \Psi' \rightarrow \gamma\chi_{1,2} \rightarrow \gamma\gamma J/\Psi \rightarrow \gamma\gamma e^+e^- \tag{1.1}$$

In case of the $p\bar{p}$, all states of the charmonium spectrum can be formed directly by

$$p\bar{p} \rightarrow \chi_{1,2} \rightarrow \gamma J/\Psi \rightarrow \gamma e^+e^- \tag{1.2}$$

and the resolution is determined by the beam quality, i.e. the momentum spread.

Another topic is the search for hybrids and glueball states. Glueballs are excited states of pure gluons, while hybrids are resonances consisting of a quark, an antiquark and an excited gluon. Gluons can couple in such a way that glueballs and hybrids may have exotic quantum numbers J^{PC}, not realized for ($q\bar{q}$) configurations. A candidate of the ground state of a glueball is the resonance $f_0(1500)$ with $J^{PC} = 0^{++}$ which was discovered by the Crystal Ball at LEAR[8] at (CERN) with a mass close to the predicted one, as shown in Fig. 1.3. There are, however, some discrepancies due to the non-flavor blind decay of this state, expected as a characteristic feature of glueballs. This result is attributed to the mixing of the glueball with neighboring mesonic states with the same quantum numbers 0^{++}. In the region of 3−4 GeV/c^2, only about 10 states are expected. That is the reason why the mixing is suppressed and a width less than 100 MeV is possible. An overview of the accessible mass range with respect to the momentum of the antiproton beam for different thresholds and specific reactions is shown in Fig. 1.4.

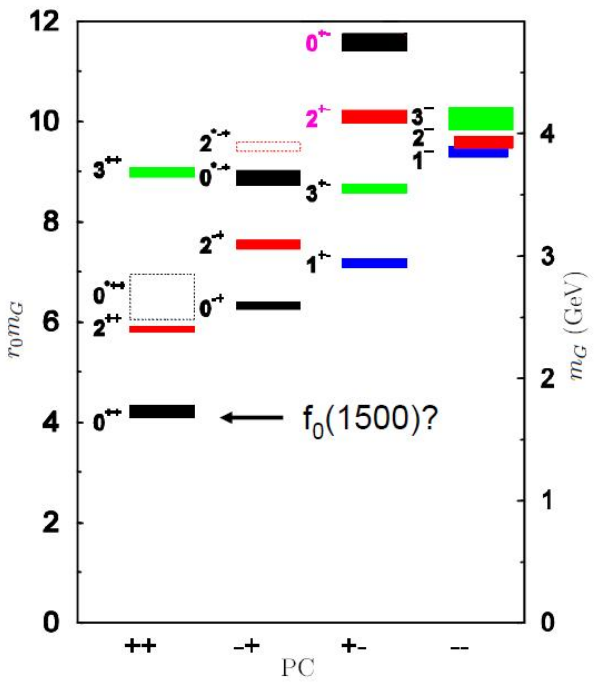

Figure 1.3: Predicted glueball spectrum from lattice QCD calculations.

For hybrid states ($q\bar{q}g_{\text{exited}}$) one has to differentiate between light quarks (u,d,s) and charmed hybrids, which are accessible near masses of 1.5 respectively 4.2 GeV/c^2. Other measurements will affect the investigation of several properties in nuclear medium, e.g. the shortening of charmed meson-lifetimes. Another interesting point is the suppression of the cross section in $\bar{p}A$ collisions for J/Ψ production which provides important information for the interpretation of heavy-ion experiments searching for the formation of a quark gluon plasma. Hyperon[9]- antihyperon pairs can also be formed in $\bar{p}A$ collisions. This allows a direct comparison of baryon and antibaryon potentials. Furthermore, hyperons can replace one or more nucleons in a nucleus to form hypernuclei. Even double hypernuclei can be formed, but here an additional step is required[10]. The existence of hypernuclei can be taken into account by adding a strangeness degree of freedom to the nuclear chart (Fig. 1.5, right). In this case, the detection of the

[8] LEAR = Low Energy Antiproton Ring
[9] baryon with at least one strange quark, but no heavier quarks (c,b,t)
[10] $p\bar{p} \rightarrow \Xi^-\bar{\Xi}^+$; Ξ^- rescatters and is stopped in secondary targets; $\Xi^- p \rightarrow \Lambda\Lambda$

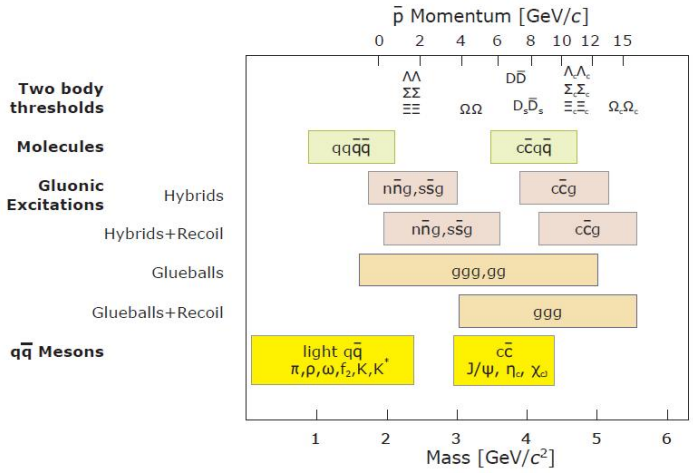

Figure 1.4: The accessible mass range with the required momentum of the antiproton beam for hybrids, glueballs, light and heavy mesons [VM].

emitted low energy photons ($\sim$ 100 keV) is the task of 8 Germanium cluster detectors (Fig. 1.5, left), which will replace the backward calorimeter EC and the micro vertex detector (MVD).

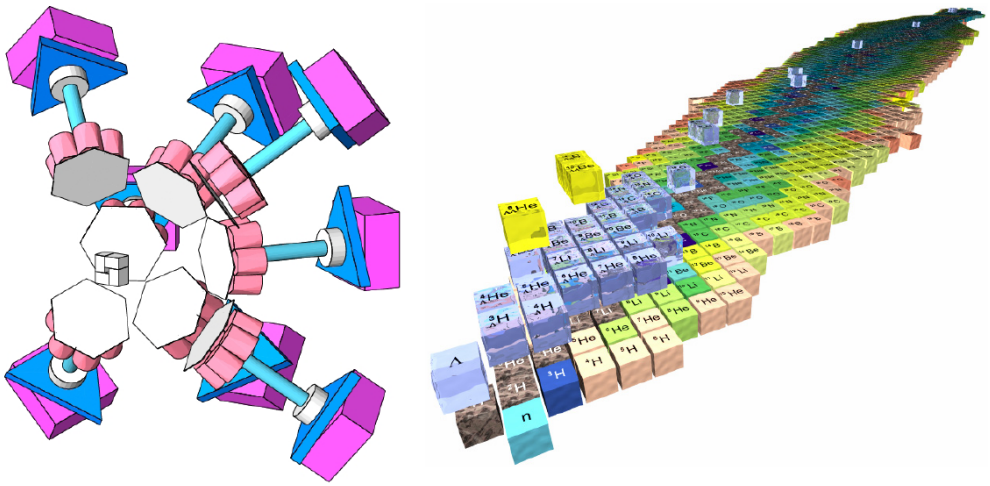

Figure 1.5: Left: Germanium cluster detectors for hypernuclei experiments. Right: Three-dimensional nuclear chart with strangeness degree of freedom [PPR].

1.2 Importance and specifications of the EMC

The design of an EMC is usually driven by the requirements of the physics program and the available budget. In case of $\overline{\mathrm{P}}$ANDA, the EMC of the target spectrometer (TS) is divided into three parts: Barrel, backward and forward EC calorimeter, which are covering different angular regions. For clarity, the following nomenclature is used:

Backward EC-EMC	BEC
Barrel EMC	Barrel
Forward EC-EMC	FEC

Table 1.1: Nomenclature of the EMC components.

The whole EMC consists of about 16000 $PbWO_4$ (PWO) crystals which are intended to be supplied by BTCP[11]. Their fabrication relies strongly on the proven technology for mass production to guarantee the necessary homogeneity. The crystals will be read out by APD[12] and VPT[13] photo detectors, respectively. Photomultipliers are excluded due to the operation in a magnetic field of 2 Tesla. The EMC is one device of $\overline{\mathrm{P}}$ANDA among other detector components which should provide necessary information of the decay products. Especially for the reconstruction of decay modes which end up in a large fraction of electromagnetic probes, it is essential to have a good calorimeter. The main requirements for the EMC are the following:

- compactness
- fast response to handle high interaction rates
- sufficient energy resolution over a large energy range (from a few MeV up to several GeV)
- radiation hardness to guarantee long operating periods

Lead tungstate is chosen as scintillator material of the calorimeter in the TS due to its sufficient resolution and fast response. Furthermore, the density of 8.28 g/cm^3 and a radiation length of 0.89 cm allow a compact design with a thickness of 20 cm which corresponds to approx. 22 X_0[14]. The short radiation length is also connected to a relatively small Molière radius (2.0 cm), which gives the scale of the transverse dimensions of the shower. For the EMC, nearly 4π solid angle coverage is envisaged for detection of multiple photon and meson decays excluding the elliptical hole in the

[11] BTCP = Bogoroditsk Techno Chemical Plant
[12] APD = Avalanche Photo Diode
[13] VPT = Vacuum Photo Triode
[14] X_0 = radiation length

most forward region of the FEC. This hole has an opening angle of 5° and 10° for the vertical and horizontal direction, respectively, to let particles pass with an extreme forward boost.
The granularity of the planned EMC provides an excellent position resolution and the point of impact can be reconstructed from the center of gravity of the electromagnetic shower distributed over the cluster of responding crystals.
Another challenge of the EMC is the handling of high interaction rates. The HESR has the capability to store 10^{11} anti-protons with a momentum of $1.5 - 15$ GeV/c and typical spread in momentum of $\frac{\Delta p}{p} = 10^{-4} - 10^{-5}$ exploiting stochastic and electron cooling techniques. With a typical target thickness this leads to a luminosity in the order of 10^{32} cm^{-2}s^{-1}. Due to the fixed target kinematics and the forward boost of the colliding particles in the laboratory system, most of them will be emitted into small angles with respect to the beamline towards the FEC. Because of the resulting high count rates, it is therefore desirable to have short decay times and thus a fast response of the crystals. In case of PWO, within 100 ns more than 95% of the generated scintillation light at the mean emission wavelength of 420 nm is collected. The readout of the crystals in the FEC is the task of VPTs, which are specified with a rate capability above 500 kHz. In comparison, an event rate between $10 - 100$ kHz is expected in the barrel. These values are visualized in Fig. 1.6.

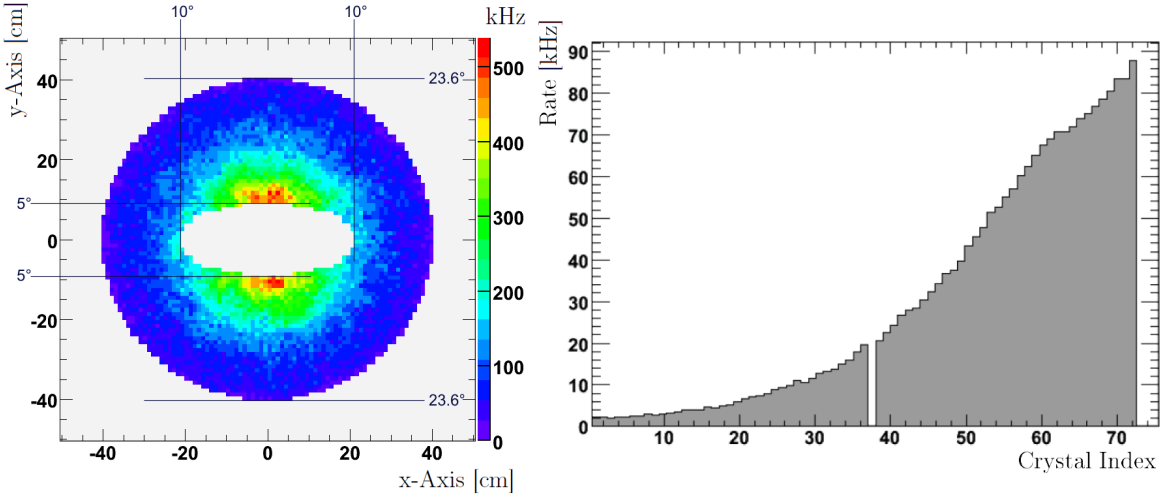

Figure 1.6: Simulations with antiprotons ($p_{\bar{p}} = 14$ GeV/c) were performed to study the expected rates in the EMC of photons with $E_\gamma > 1$ MeV [TDR]. Left: Rate distribution for the FEC. Right: Rate distribution for the barrel. Index 0 refers to the most backward angle (140°) and index 72 to the to the most forward angle (22°) in the barrel. The hole at index 37 corresponds to the opening for the pellet target.

These rates might be even exceeded due to fluctuations in the beam intensity. Large Area APDs are foreseen to read out the crystals in the barrel part of the EMC with

a low-energy photon threshold of 10 MeV[15].
On the one hand, a main challenge of the EMC is to have a sufficient detection efficiency over a large energy range. It is important to identify photons at low energies from e.g. asymmetrically decaying background channels like $\bar{p}p \rightarrow \pi^0\gamma$, $\bar{p}p \rightarrow \pi^0\eta$ or $\bar{p}p \rightarrow \pi^0\pi^0$ to increase the signal-to-background ratio. But on the other hand, the EMC should also have a relatively good resolution at lower energies for the reconstruction of these photons in an invariant mass spectrum. As an example for the necessity of good reconstruction of decay products, the two decay modes of the searched hybrid state X(1^{-+}) are shown in Fig. 1.7.

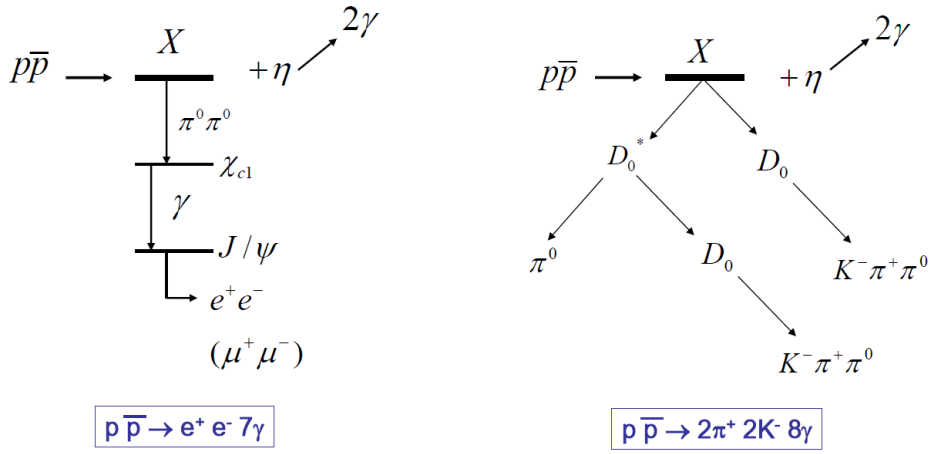

Figure 1.7: The figure shows the two main decay modes of X(1^{-+}). The summary of products in the final state, especially the large number of photons, emphasizes the importance of a good electromagnetic calorimeter due to the reconstruction of these channels [VM].

The different parts of the EMC are designed to have specific dynamic ranges according to the kinematics of the detected particles and photons:

BEC	10 MeV - 0.7 GeV
Barrel	10 MeV - 7.3 GeV
FEC	10 MeV - 14.6 GeV

In general, the dependence of energy resolution on the incident energy is given by:

$$\sigma_E/E = a \oplus \frac{b}{E[GeV]} \oplus \frac{c}{\sqrt{E[GeV]}}. \tag{1.3}$$

[15] 3 MeV energy threshold for a single crystal

The meaning of the coefficients are in the following:

a	non-uniformities, shower leakage
b	electronics term
c	photoelectron statistics, shower fluctuations

In the technical design report (TDR) of the EMC [TDR] the required performance value for the energy resolution is given by:

$$\sigma_E/E \leq 1\% \oplus \frac{\leq 2\%}{\sqrt{E[GeV]}} \tag{1.4}$$

Due to the low light output of PWO at room temperature it was decided to operate at $T = -25°C$ to increase the photoelectron statistics and for this reason an improvement of the energy resolution by a factor of roughly 2 is achieved.
Radiation damage reduces the output of the scintillation light and therefore the number of photoelectrons per unit of deposited energy. This originates from a reduction of the optical transmission of the crystals due to the formation of colour centres. An interplay between irradiation and recovery leads to an asymptotic effective loss of the light yield (LY) with increasing damage or totally absorbed dose. That is the reason why cooling down the crystals to $T = -25°C$ causes also a significantly reduced light output because of the deceleration of the recovery processes. To guarantee a long operation period of the detector, a sufficient radiation hardness is required. For the mentioned reasons, dose rates up to 20-30 mGy/h are expected for the most forward region of the FEC. This corresponds to an integral dose of 65 Gy for a continuous runtime of half a year. For the majority of the barrel the expected values are about two orders of magnitude lower. In contrast to the FEC, this requirement is not predicted as a problem for the barrel part due to the low dose rates in this region. The radiation hardness of the EMC itself is determined by the radiation hardness of the individual crystals and is specified by the radiation induced changing of the absorption coefficient Δk for a given integral dose.

1.3 Further development of PWO to PWO-II

Generally, PWO meets the requirements to be an extremely fast, compact and radiation hard scintillator, but for the applications of $\overline{\text{P}}$ANDA a couple of improvements were necessary, especially with respect to the light output. The most crucial parameters are the light yield, radiation hardness, fast scintillation kinetics and large-scale production. As a first stage of R&D[16], several kinds of dopings were tested to improve

[16] R&D = Research & Development

the light yield. For low-energy photons the best results were achieved for crystals with a doping of molybdenum (Mo) and lanthanum (La) at concentrations < 100 ppm, but in addition with the drawback of a longer decay time, both shown in Fig. 1.8. The

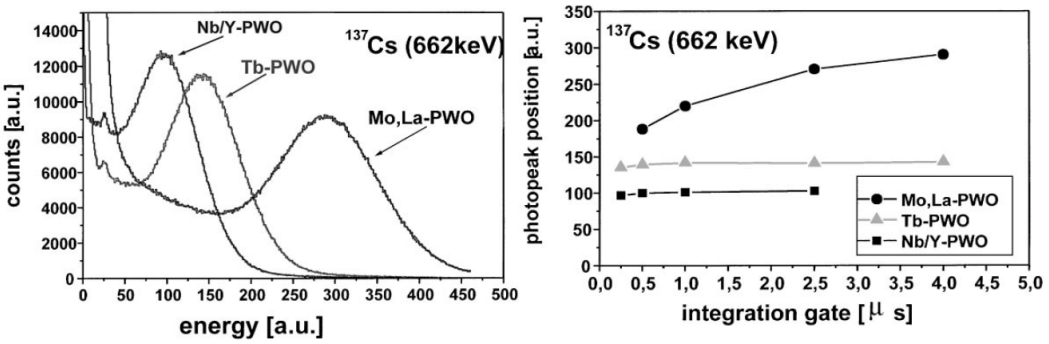

Figure 1.8: Left: Energy response of low-energy (662 keV) photons measured for PWO-samples with different kind of doping. The Nb/Y-doped sample stands for a crystal which fulfills CMS specifications. Readout was done by a usual Photomultiplier. Right: Dependence of the photopeak on the integration time [AA].

appearance of this slow scintillation component of $\tau = 1 - 4\ \mu s$ limits the application at high counting rates. A further improvement of the light yield of 30% - 50% can be achieved by a combination of the reduction of the La- and Y-concentration to a level of ~ 40 ppm and an improved control of the stoichiometric composition of the melt. Because of the different distribution coefficients, lanthanum and yttrium are concentrated in the seed and the bottom part respectively. To avoid this unbalance, these doping ions are introduced into the crystal at different stages of the raw material preparation and crystal growth. Both innovations lead to a significantly lower level of vacancies and therefore to an increased light yield of about 80% in comparison to a CMS crystal. In the following, this type of crystal will be named PWO-II. This type shows a clear dominance of the fast decay component at 97% and a decay time in the one-digit ns-region, measured at room temperature.
Furthermore the light yield can be significantly increased by cooling down the crystals. This effect is a general property of lead tungstate and not specific for PWO-II and is due to the thermal quenching of the luminescence process. The increase of the light yield varies nearly linearly with a change of the temperature -3 %/K in the relevant temperature region, which is shown in Fig. 1.9. Decreasing the temperature to $-25°$C also has a tolerable impact on the kinetics of the scintillation process but becomes only slightly visible. Fig. 1.10 shows several normalized measurements of the light output at different temperatures. Another important point is the availability of radiation harder crystals due to the operation at $-25°$C and the dominance of slow recovery components. The light loss becomes critical at the inner FEC region because of the high dose rates, but can be taken over by extremely radiation hard crystals

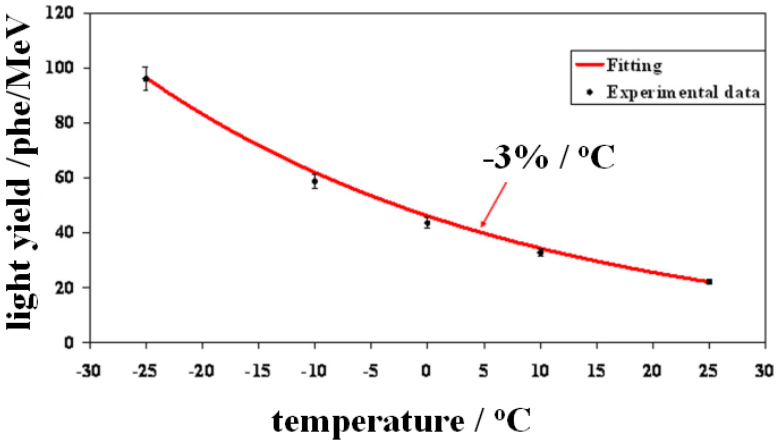

Figure 1.9: Change of the light yield output with respect to the temperature. The light yield gradients stays nearly constant at -3 %/K [TDR].

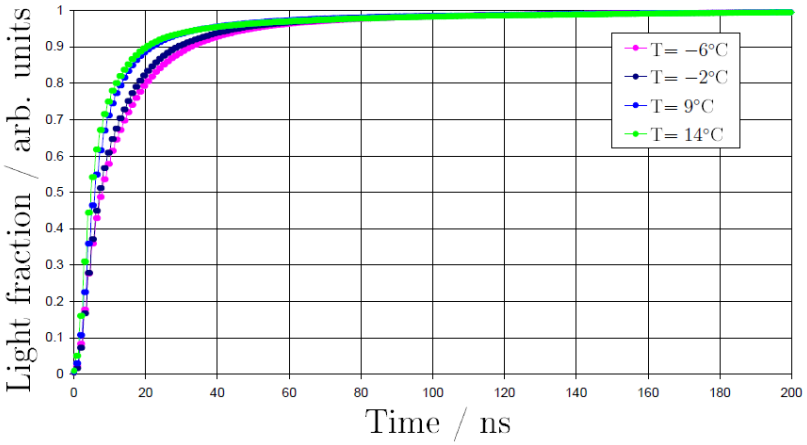

Figure 1.10: Measurements of the total light yield collected within increasing time gates measured at temperatures between -6 and $+14$°C. Only a small change of the kinetics becomes visible within the first 50 ns [KIN].

selected at room temperature [NOV2]. Fig. 1.11 shows a linear correlation between the light loss at −25°C and the induced absorption at room temperature.

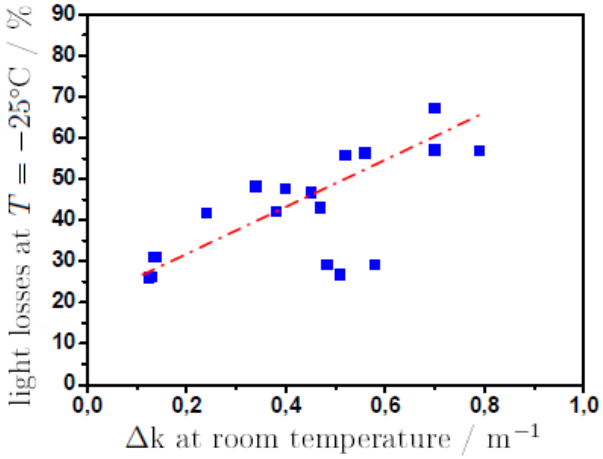

Figure 1.11: Correlation between light losses and Δk at −25°C and room temperature, respectively, after an integral dose of 52 Gy. The large range of light loss between 20% and 70% is conspicuous. For that reason only extrem radiation hard crystals are suitable for the inner FEC region [NOV2].

Altogether one can gain roughly a factor of 8 in the LY in comparison with PWO at +25°C (ECAL of CMS) to PWO II at −25°C ($\overline{\text{P}}$ANDA EMC). Latest prototype tests (at MAMI[17] in Mainz) operating at −25°C with a 6 × 10 matrix of PWO II crystals show a good energy resolution which is illustrated in Fig. 1.12.

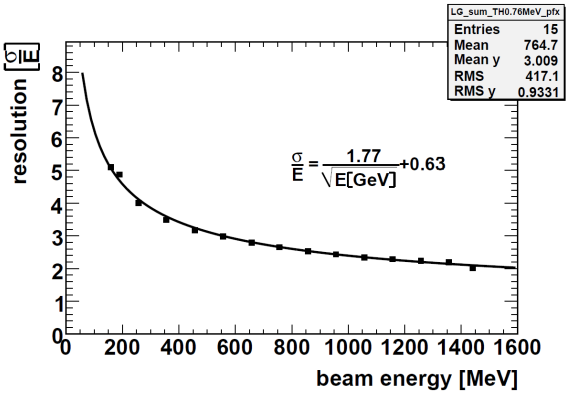

Figure 1.12: The figure shows the achieved energy resolution of the PROTO 60 with similar conditions as in the $\overline{\text{P}}$ANDA experiment. In this case, all of the 60 crystals were used to reach the best possible energy resolution [MAMO].

[17] MAMI = MAinzer MIkrotron

Chapter 2

Quality Control

Quality control is a collective term for different arrangements for securing the defined requirements. The first step of quality inspection is to find a procedure which gives results from where one can judge if the required minimum quality was achieved or not. For the $\overline{\text{P}}$ANDA EMC, it was decided to have a couple of measurements from different facilities to be able to do cross checks. Therefore, different ways of measuring, which can give rise to inconsistencies, should be taken into account. This chapter is about the aims of the quality control for the EMC crystals, a way to handle these large number of quantities and it ends with the defined conditions of the properties in the contract.

2.1 Achievable limits

The achievable quality for the lead tungstate crystals are specified in absolute numbers which are based on experience and the way of manufacturing. Presently the world's largest lead tungstate crystal producer BTCP produces crystals by the Czochralski method. Crystals are grown from raw material with a purity level close to 6N[1] specification and an additional precrystallization step for producing high quality crystals. Ingots with a slightly elliptical cross-section and a length of 25 cm (Fig. 2.1) are used to produce the crystals. This way of manufacturing was developed and specialized to achieve the optimum parameters for the $\overline{\text{P}}$ANDA EMC. Based on the physical goals and also for the mechanical integration, the crystals should reach minimum requirements. For example the size of an individual edge should not exceed the defined limit to fit into the carbon alveoles. Also the transmission, light yield, the kinetics of the scintillation process and the radiation hardness should be sufficient to guarantee an efficient EMC. The limit for each parameter was chosen with respect to previous experiences and detailed studies. A secondary effect, which comes up by manufacturing large numbers of quantities, is the appearance of Gaussian-like distributed values.

[1] $\geq 99.9999\%$

Figure 2.1: Lead tungstate ingots to produce modules in $\overline{\text{P}}$ANDA geometry for the FEC [TDR].

Therefore, from case to case some crystals in a tail of a distribution can be out of specification. But on the other side such a tail can also show up for excellent crystals. In case of the radiation hardness, it is desirable to have a significantly high amount of crystals with relatively low Δk-values, which will be mounted in the most forward region of the FEC. For this reason, a second condition concerning the distribution of the Δk-values is required. The mean value for each lot should be less or equal 0.75 m^{-1}.

2.2 Homogeneity

As it was mentioned in the previous section, the parameters of the crystals are statistically distributed. Preferably, one wants to have a preferential homogeneous calorimeter to avoid additional steps of calibration to correct for local deviations or fluctuations. That is the reason why it is desirable to have very narrow distributions. This fact is again connected to the way of manufacturing. In spite of sufficient narrow distributions a couple of calibration steps will be necessary and performed to guarantee the ultimate performance of the EMC. An energy resolution of less than 2% at 1 GeV requires calibration at the sub-percent level. This is reachable via a combination of three methods:

- pre-calibration with cosmic muons
- in situ calibration with physics events
- continuous monitoring with a light-pulser system

2.3 Correlations between room temperature and −25°C

The final EMC of the $\overline{\text{P}}$ANDA detector will be installed in an environment which is cooled down to −25°C. For the quality control it would not be economical to perform the hole test procedure at similar conditions for each single crystal. For that reason linear correlations are necessary between parameters measured at room temperature and −25°C, respectively. One important correlation was already shown in 1.11 in chapter 1.3. The figure shows the linear correlation between the light loss at −25°C and the measured Δk value at room temperature after an integral dose of 52 Gy. This relation confirms the selection criteria for sufficient radiation hardness for those crystals exposed to the maximum dose during experiment.
Another important and also strongly temperature dependent property of the crystals is the absolute LY. There are a lot of publications which show the clear linear correlation between the LY of lead tungstate at +25°C and −25°C to argue for the final operating temperature. Within the light yield calibration, which is discussed in detail in subsection 3.3.2 additional measurements were performed to confirm this dependence once more. Fig. 2.2 shows the linear correlation between −25°C and +18°C. The latter temperature is the relevant one for the usual calibration measurements with respect to the contract.

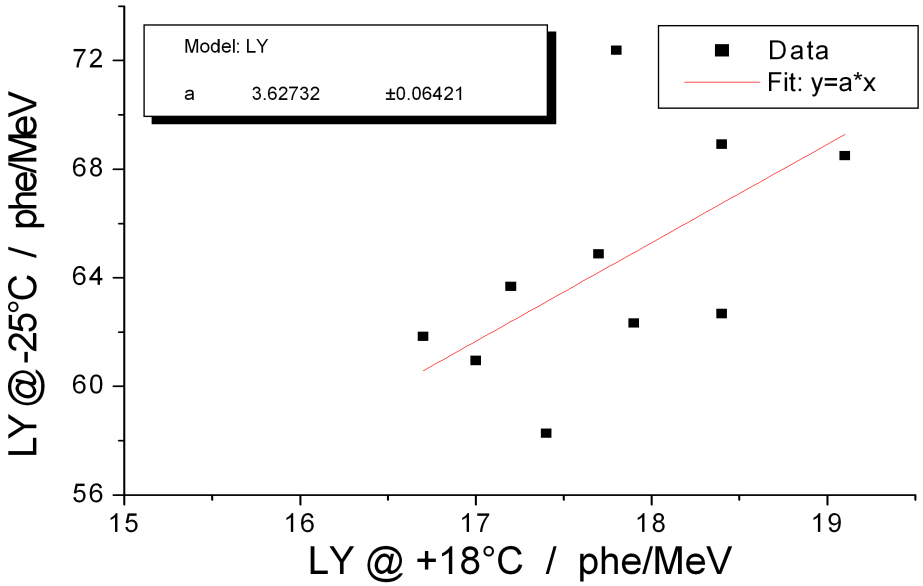

Figure 2.2: Correlation of LY between −25°C and +18°C. The fitted gain factor of 3.63 is consistent with the gain factor of ∼ 4 for the temperature difference from −25°C and +25°C.

2.4 Choice of the specification limit concerning radiation hardness

The main difference between the chosen specification limits of $\overline{\mathrm{P}}$ANDA and CMS concerning the radiation hardness at 420 nm originates from the different energy ranges which is in case of the LHC[2] roughly two orders of magnitude higher. For the quality control of the radiation hardness CMS chose an integral dose of $\geq$ 500 Gy with a minimum dose of 100 Gy. Within these conditions the induced absorption of a crystal, which should not exceed 1.5 m^{-1}, reaches full saturation due to the interplay of radiation damage and recovery. Concerning $\overline{\mathrm{P}}$ANDA, a maximum tolerable change of the absorption coefficient of 1 m^{-1} was chosen after an integral dose of 30 Gy. This condition corresponds to approximately 80% - 85% of saturation (Fig. 2.3) and to a runtime of half a year in the most forward region of the FEC. Therefore one knows the expected light loss after this period because of the change in transmission (compare Fig. 1.11).

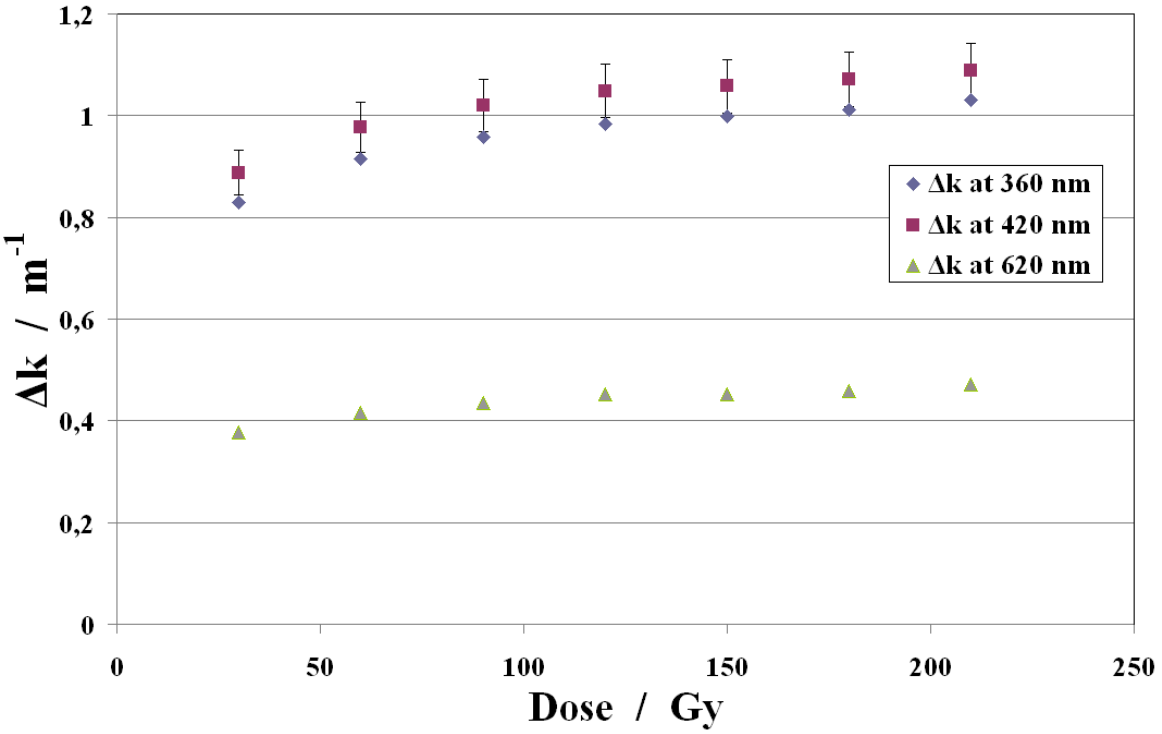

Figure 2.3: Saturation curve of a lead tungstate crystal depending on the deposited dose at 3 different wavelengths [VD].

[2]LHC = Large Hadron Collider

2.5 Conditions for the contract

The $\overline{\text{P}}$ANDA requirements for the crystal quality according to the contract are listed in Tab. 2.1 and are more stringent mainly due to the requested higher light yield and the operation at low temperature down to T= −25°C.

Property	Unit	Limit
longitudinal transmission at 360 nm	%	≥ 35
longitudinal transmission at 420 nm	%	≥ 60
longitudinal transmission at 620 nm	%	≥ 70
non-uniformity of transversal transmission at T= 50%	nm	≤ 3
LY at T= 18°C, polished crystal	phe/MeV	≥ 16.0
LY(100 ns)/LY(1 μs)		≥ 0.9
induced absorption coefficient Δk at room temperature, integral dose 30 Gy	m^{-1}	≤ 1.0
mean value of Δk distribution for each lot of delivery	m^{-1}	≤ 0.75

Table 2.1: Relevant specifications of the crystals for the $\overline{\text{P}}$ANDA EMC.

Chapter 3

Procedure of Quality Control

The procedure of quality control of the crystals for the $\overline{\text{P}}$ANDA EMC is the task of three facilities. The first quality check of the crystals is performed by the provider BTCP in order to avoid the delivery of crystals with insufficient quality. Secondly, each lot is shipped to CERN to pass the next station of quality control. Both, BTCP and CERN, are using a similar device to test the crystals, which was already used for the ECAL of the CMS experiment: Automatic Crystal Control System (ACCOS), shown in Fig. 3.1. Considering the different geometry of the $\overline{\text{P}}$ANDA crystals compared to CMS, those ACCOS machines had to be modified for the test procedure. The final inspection, absolute calibration of the LY, as well as the determination of the radiation hardness are performed at Gießen. For different reasons not all properties of

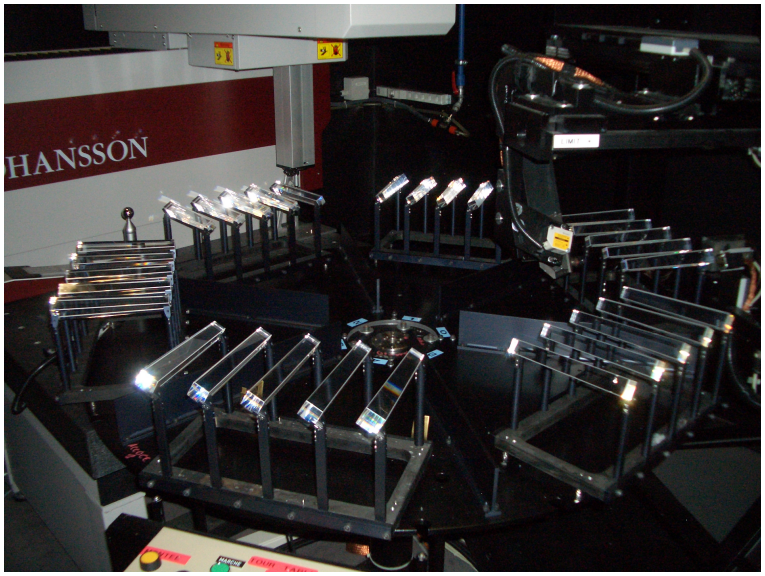

Figure 3.1: A picture of the round server of the ACCOS machine which serves the reference and test crystals for the different test stations.

Property	BTCP	CERN	Gießen
geometries	√	√	×
longitudinal transmittance	√	√	√
transversal transmittance	√	√	×
light yield	√	√	(√)
scintillation kinetics	√	√	×
radiation hardness	√	×	√

Table 3.1: Overview of the quality control of the crystals and where they are tested. Only for a few random crystals of each lot the LY was measured in Gießen to determine the calibration coefficients.

the crystals are measured at each facility. Therefore, Tab. 3.1 gives a short overview of the parameters tested at each facility.

3.1 Geometry

The general geometry of the crystals is a tapered parallelepiped in order to reduce the dead zone effect, in comparison with completely straight crystals in particular to achieve a hermetically closed barrel geometry. In addition to the crystal shape of the forward and backward EC, there are 11 different crystal geometries differently tapered for the coverage of the angular regions in the barrel part. A mirror symmetry (plane perpendicular to the beam and containing target point) allows the reduction from originally 18 to 11 different types of crystals. Due to the symmetry of the 16 barrel slices all 11 shapes are produced in 2 versions symmetric to one of the side faces. The mechanical drawing and the definition of all geometrical parameters are shown in Fig. 3.2 and Table 3.2 [TDR]. One crystal has an average mass of roughly 1 kg and a length of 20 cm which corresponds to 22 X_0. To guarantee the mechanical integration into the foreseen carbon alveoles, all given dimensions in Fig. 3.2 have a maximum tolerance of $0/-0.1$ mm which is based on the experiences of the achievable precision for the CMS calorimeter. Other requirements concerning the geometry are the following:

- All surfaces are polished with a roughness ≤ 0.02 μm.
- The edges should have a roughness of no more than 0.5 μm.
- No cracks deeper than 0.5 mm are allowed.

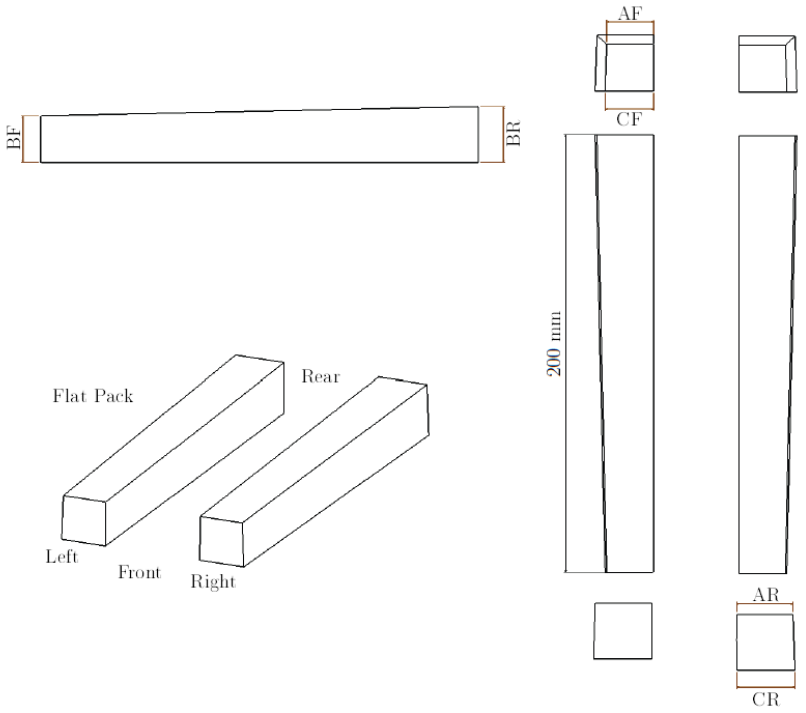

Figure 3.2: Mechanical drawing of the lead tungstate crystals. All crystals have a right angle corner in order to simplify the design and to reduce machining costs.

Type	Volume cm^3	AF	BF	CF	AR	BR	CR
		mm					
1	126.86	21.21	21.28	21.27	29.04	28.75	29.12
2	126.56	21.18	21.28	21.39	28.78	28.75	29.07
3	125.79	21.17	21.28	21.51	28.36	28.75	28.81
4	120.85	21.17	21.28	21.60	27.90	27.22	28.45
5	119.69	21.17	21.28	21.69	27.35	27.22	28.01
6	118.35	21.19	21.28	21.78	26.72	27.22	27.47
7	112.90	21.22	21.28	21.86	26.23	25.47	26.99
8	111.75	21.23	21.28	21.91	25.70	25.47	26.51
9	110.52	21.23	21.28	21.95	25.14	25.47	26.00
10	107.01	21.25	21.28	21.00	24.70	24.42	25.56
11	106.25	21.25	21.28	21.02	24.35	24.42	25.23
EC	126.88	24.38	24.38	24.38	26.00	26.00	26.00

Table 3.2: Definition of the geometrical parameters of the lead tungstate crystals. The EC geometry corresponds to crystals for the FEC.

All dimension measurements at CERN and BTCP are performed by a commercial 3D laser machine[1] which provides three spatial coordinates for each point with a precision of ± 5 μm. These coordinates can be used for subsequent calculations of the geometry and planarity of the crystals.

3.2 Optical transmission

The measurement of the optical transmission is divided into two parts: along and perpendicular to the long crystal axis. Lead tungstate grown according to the Czochralski method is an uniaxial negative birefringent system which causes a higher transversal index of refraction than in the longitudinal direction. The longitudinal transmission will limit the overall collected light yield of scintillation light. With the measurements of the transversal transmission, which will be taken at several points along the axis, one can make a statement on the non-uniformity of the crystals. Both kinds of transmission are tested at CERN and BTCP, but only the longitudinal one is also measured at Gießen.

3.2.1 Longitudinal transmission

The emission spectrum of the presently used quality of lead tungstate has a mean value at 420 nm and follows a Gaussian-like distribution. Therefore, the optical transmittance in that range of wavelength is essential for the detector performance. The emission spectrum extends close to the absorption edge. Its position in the individual crystals has a strong impact on the overall light yield and even shows a correlation due to the sensitivity of impurities [CMS1]. Fig. 3.3 shows a comparison between the emission spectrum of lead tungstate and a natural transmission spectrum before any irradiation. In case of the quality control, to judge whether a crystal has sufficient transmission or not, one has to compare the measured values with the specification limits at three selected and very sensitive wavelengths: 360, 420 and 620 nm.
Due to the close distance to the absorption edge, the requirements for the transmission at $\lambda = 360$ nm were chosen to avoid a cutting of the Gaussian distributed emission spectrum. Within the development of lead tungstate it was aimed to have an optimum coverage of the emitted light by shifting the natural absorption edge which is well below 350 nm successively to lower wavelengths via doping as well as reduction of defects. The mentioned correlation with the LY is another evident point for requiring sufficient transmission at this wavelength. The importance of the transmission at the mean value 420 nm is self-explanatory. 620 nm is chosen as the longest relevant wavelength due to the gain of scintillation light from the right part of the distribution and

[1] TOPAZ 7 supplied by Johansson AB (Sweden)

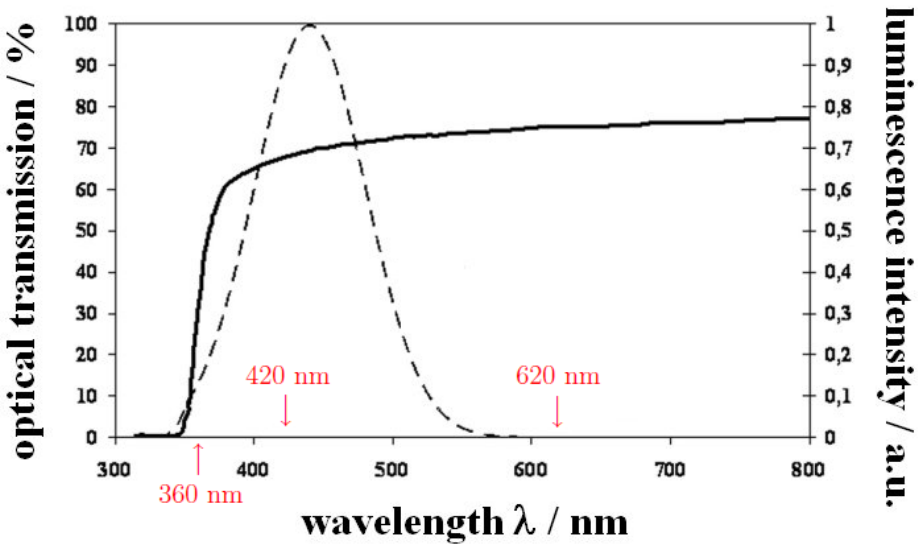

Figure 3.3: A comparison between emission (dashed curve) and transmission spectra (solid curve) of a typical 20 cm $\overline{\text{P}}$ANDA crystal with the three relevant wavelengths marked in red. The gain of the emitted scintillation light relies strongly on the transmission of the crystal itself.

to indentify any expected absorption bands such as due to Molybdenum-complexes. The upper limit for the transmission of light of an external source, without absorption and only including reflection, depends on the index of refraction. Fig. 3.4 schematically explains the origin of the individual contributions, which will be detected by a spectrometer in case of a sample with parallel entrance and exit surfaces. By summing

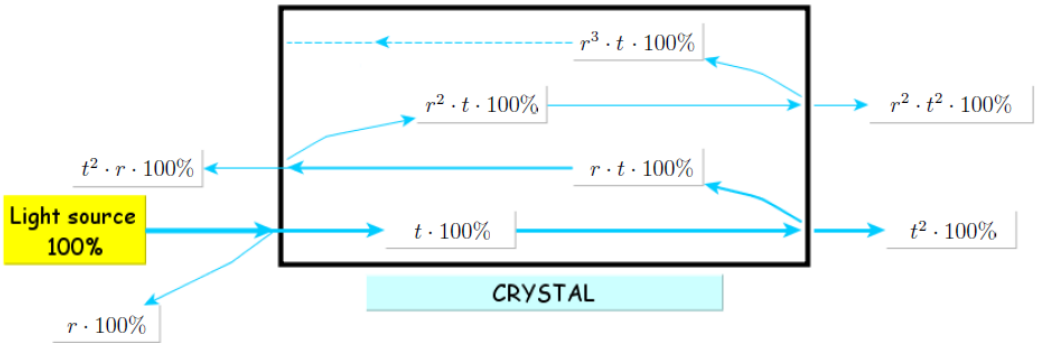

Figure 3.4: r is the fraction of intensity which will be reflected and t is the complementary value of r to 1.

up the contributions which pass across the right surface in Fig. 3.4, one can deduce the equation for the theoretical maximal transmission. This can be simplified by an

approximation to a geometrical sum and with $t = 1 - r$.

$$T_{\max} = 100\% \cdot t^2 \cdot \left(1 + r^2 + r^4 + ..\right) = 100\% \cdot \frac{1-r}{1+r} \tag{3.1}$$

r can be calculated by the optical Fresnel equations and is given for a perpendicular entrance to the crystal by $r = \left(\frac{n_{Cry}-n_{Air}}{n_{Cry}+n_{Air}}\right)^2$ [POH]. As an example, the maximum theoretical transmission at 420 nm with a corresponding index of refraction of $n = 2.24$ (given by [BAC]) is $T_{\max}^{420\text{ nm}} = 74.45\%$. All these considerations are based on the published dispersion of the index of refraction. It is assumed but not confirmed that the value for PWO-II are identical.

3.2.1.1 Setup for measurements at CERN and BTCP

CERN and BTCP use the ACCOS machine to measure the properties of each individual crystal. Fig. 3.5 shows a top view of the ACCOS machine which is composed of the dimension measuring machine, the optical bench and a circular server with a diameter of 1.1 m. The server itself consists of a turntable driven by a step motor and is able to carry 30 crystals simultaneously including the reference crystals. After measurement, all results are stored in a database [CMS5].

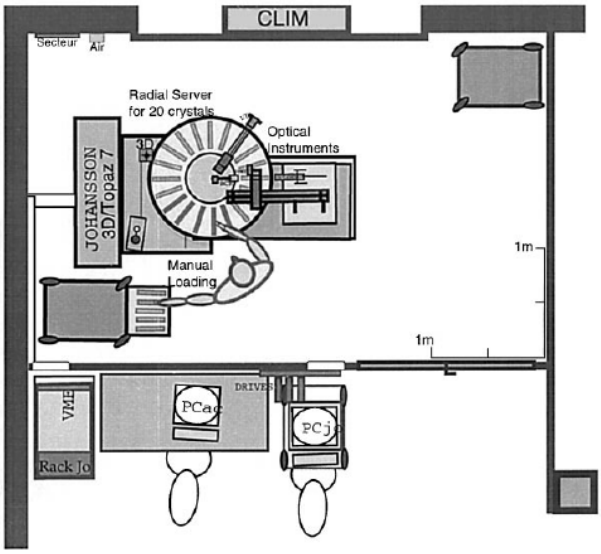

Figure 3.5: Schematic top view of the ACCOS machine [ACC].

The longitudinal transmission is measured by a spectrometer which is using a large area photodiode as detector. To speed up the measurements, the transmission is only taken at several selected wavelengths: 330, 340, 350, 360, 380, 405, 420, 450, 492, 620 and 700 nm. These wavelengths are realized by a set of narrow band pass filters. To make a statement concerning the relevant wavelengths for the requirements, all data taken for each crystal is fitted by

$$T(\lambda) = e^{-e^{-(\lambda - P_0)P_1} \cdot P_2 \cdot (1 - P_3 e^{-\lambda/92\text{ nm}})} \tag{3.2}$$

for the calculation of $T(360\text{ nm})$, $T(420\text{ nm})$ and $T(620\text{ nm})$ [CMS6]. This technique is used to measure a transmission spectrum in the range from $330 - 700$ nm in less than 10 seconds for one spatial point.

3.2.1.2 Setup for measurements at Gießen

Fig. 3.6 shows the spectrometer Cary 4000 (supplied by VARIAN) which is used for measuring the transmission. It has an accessible wavelength range from $175 - 900$ nm and works with the standard two-beam technique. One serves as reference beam and the other one passes through the sample. According to the measured range from $300 - 900$ nm, only the halogen bulb (lifetime ≈ 1000 h) is used for the visible range. Furthermore, the spectrometer is equipped with a monochromator, lenses, mirrors, a detector and a sample compartment. Unfortunately, the width of the compartment is

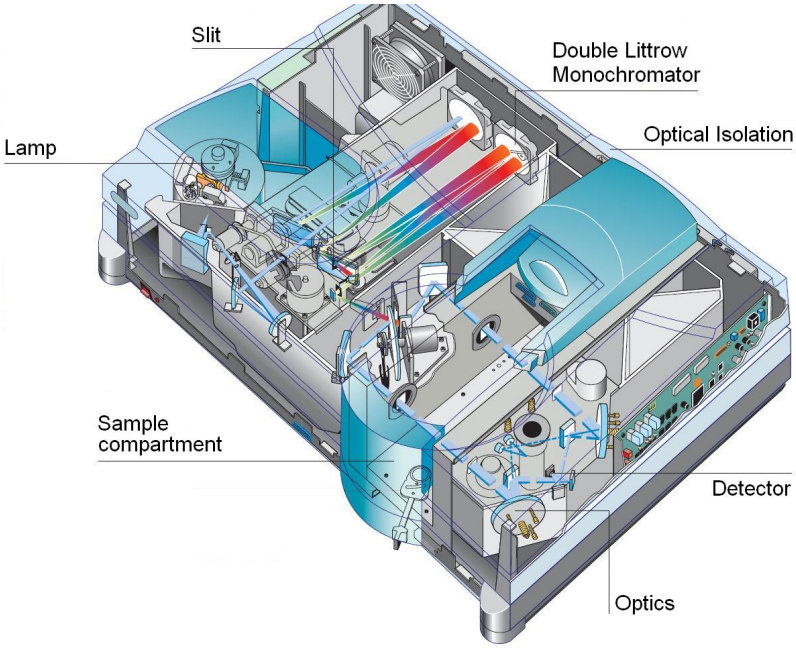

Figure 3.6: The figure shows a schematic view of the VARIAN Cary 4000 spectrometer. To measure along the full length of the crystals, additional optics are installed in the compartment which are not drawn here [VAR].

too short to measure along the full length of the crystal (20 cm). For that reason an additional optical setup[2] (Fig. 3.7, left) was designed to deflect the beam out of the compartment, across the crystal and back to the sensor and to provide in contrast to the standard performance a nearly parallel beam with a negligible divergence. Due to the additional mirrors and lenses, the intensity of the sample beam is decreased by more than one order of magnitude and therefore also the ratio between the intensity of sample and reference beam (baseline). Before performing any measurement this ratio is recorded each time and is automatically taken into account by the software to avoid the influence of thermal and voltage fluctuations or any other uncertainties

[2]provided by the HUND company, Wetzlar

depending on the wavelength. The comparison of the baseline with and without the additional optics for bending is shown in Fig. 3.7 (right). Consequently the spectrometer is much more sensitive to small shifts in the baseline during measurements, but due to its high sensitivity still absolutely sufficient for the application. Every

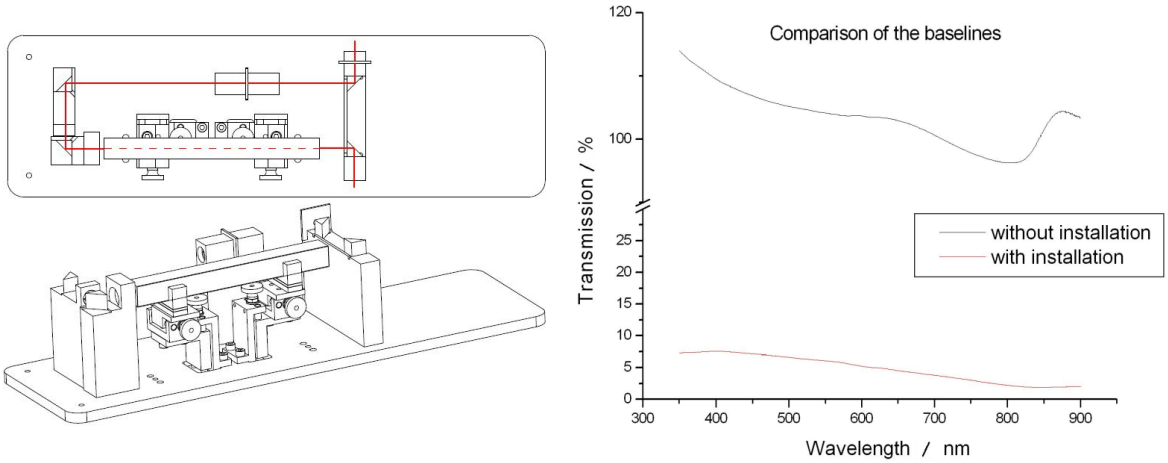

Figure 3.7: Left: The additional optic setup for deflecting the beam [HUN]. Right: A lot of light is lost during deflecting the light out and back to the compartment because of losses by mirrors and slits.

crystal is measured within a range of $325 - 900$ nm in steps of 0.5 nm. The spectral bandwidth (SBW) of the spectrometer is 5 nm and the scan rate is 300 nm/min which corresponds to roughly 3 min for one full spectral scan. More detailed information about the spectrometer can be found in [VAR].
The transmission measurements also bring up some uncertainties. One small contribution is due to the not exactly reproduceable position of the crystal in the spectrometer in spite of the attachment points. Another fraction originates from a shifting of the baseline because of obviously thermal effects which causes directly a change in the transmission. It was decided to remeasure the baseline after a deviation of 0.1% from the 100%-line without a sample. To get a rough estimate of the sum of both errors, several measurements were taken with the same crystal. One can assume the following errors for the relevant wavelengths: $\Delta T(620\text{ nm}) = \Delta T(420\text{ nm}) = 0.4\%$ and $\Delta T(360\text{ nm}) = 0.8\%$.

3.2.1.3 Model for light propagation in a lead tungstate crystal

In order to get a rough estimation of the fraction of multiply reflected photons in a crystal and to have a cross check with the theoretical prediction, simulations were performed within the LITRANI framework [LIT1, LIT2]. It is a Monte-Carlo based ROOT[3] add-on which is written in C++ and was developed to simulate light propagation in isotropic and anisotropic media. Before starting the simulations, several input parameters are to be included in the program. First of all, the setup which is implemented should be similar to the real one (Fig. 3.8). The photons are generated

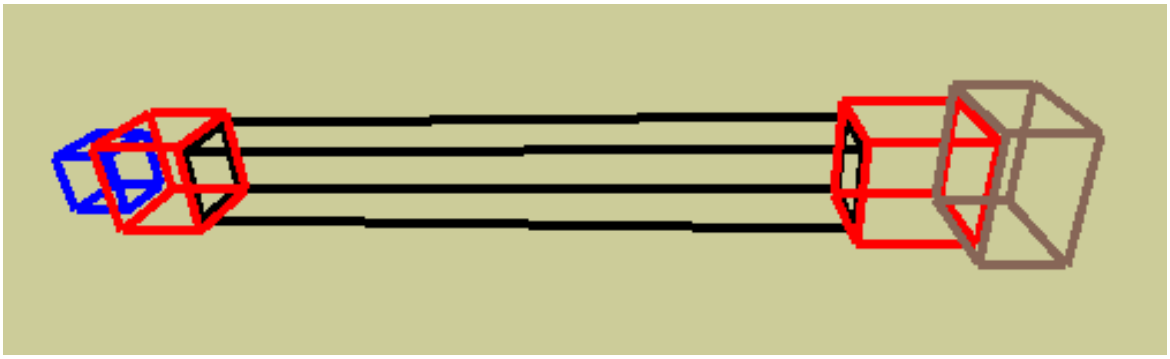

Figure 3.8: The setup for simulation of light propagation. The different shapes represent the following: light source (blue), air gaps (red), crystal (black), detector (brown)

from a light source with elliptical shape with semi-axis of 1.5 and 3 mm respectively, and with a small divergence of approximately 0.3° which is placed in the center of the blue shape in Fig. 3.8. These values were determined from an engineering drawing and intensity distributions provided by the HUND company, shown in Fig. 3.9. Both air gaps were inserted to be sure to have a change of index of refraction at these planes. All other faces of the crystal are surrounded by a thin slice of air to take into account total reflection and refraction. The setup is embedded into a completely absorbing material to stop those photons which will never reach the detector. The detector is simplified and realized by a cuboid of which one surface is sensitive to the detection of photons with a perfect quantum efficiency (QE) equal to 1. It is reasonable to choose QE= 1 due to the baseline correction and normalization of the VARIAN spectrometer. As a first approximation lead tungstate was taken as an isotropic medium for checking the reproducibility of the maximum transmission value by artificially varying the absorption length in the order of 100 m and a longitudinal index of refraction given by [BAC]. The result is shown in Fig. 3.10.
The final absorption length implemented into the simulation originates from the experimental transmission data (before and after irradiation respectively) and is calculated

[3]ROOT is an object-oriented program and library developed by CERN

with equation 3.3 which was published in [BAC] and comprises also photons which are multiply reflected. r and t have here the same meaning as described in Fig. 3.4.

$$T_{\mathrm{Exp}} = \frac{t^2 e^{-d/l_{\mathrm{abs}}}}{1 - r^2 e^{-2d/l_{\mathrm{abs}}}} \tag{3.3}$$

$$\Rightarrow l_{\mathrm{abs}} = \left[\frac{-1}{d} \cdot \ln \left(\frac{-t^2 + \sqrt{t^4 + 4T_{\mathrm{Exp}}^2 r^2}}{2T_{\mathrm{Exp}} r^2} \right) \right]^{-1} \tag{3.4}$$

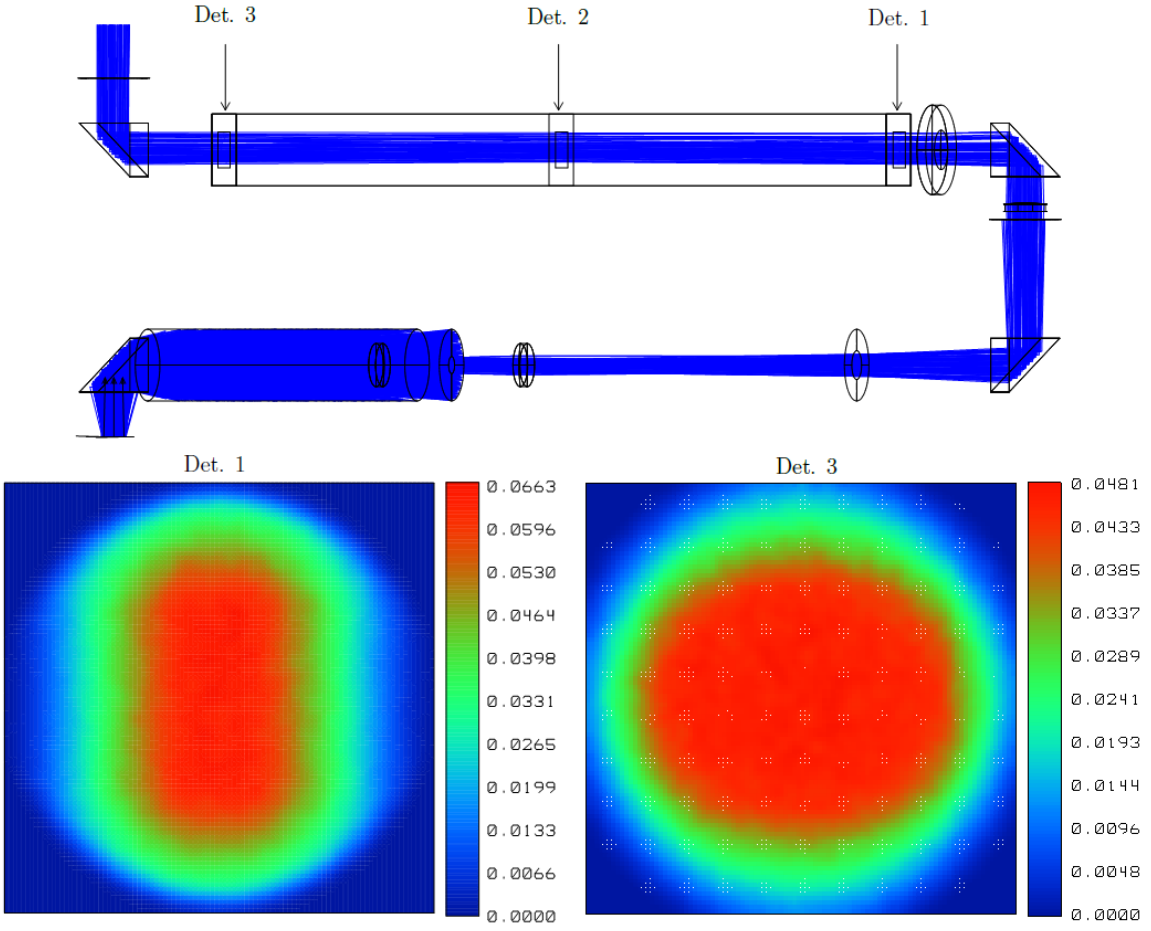

Figure 3.9: The upper picture shows the path of the deflected beam and the positions of the virtual detectors (10×10 mm^2) for controlling the ingoing and outgoing intensity of the beam in [HUN].

A change of the geometry of the crystal has no significant impact on the final results due to the small beam divergence and the co-planarity of both end faces for each type of crystal geometry. To distinguish whether a photon was reflected or not is

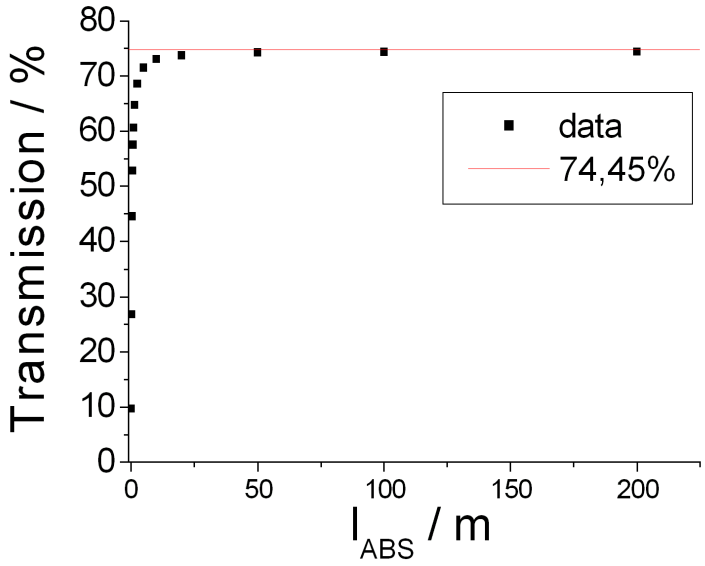

Figure 3.10: At artificial long absorption length with therefore negligible absorption the simulated values saturates at the expected maximal value for the transmission.

shown in 3.11. Both spectra show the number of photons versus the travel time from emission until final arrival in the detector. The equal distances between the peaks are caused by the multiple pathlength of reflected photons. Finally, the fraction of multiply reflected photons is directly given by the ratio between the integrals of the corresponding peaks. The results of several runs for different crystals give an average value of about 2% for the ratio beween multiple reflected photons and those which pass once through the crystal. This is in agreement with the theoretical prediction. These simulations are primarily used to estimate the systematic error of Δk, the change of induced absorption coefficient, due to radiation damage and will further be discussed in section 3.5.

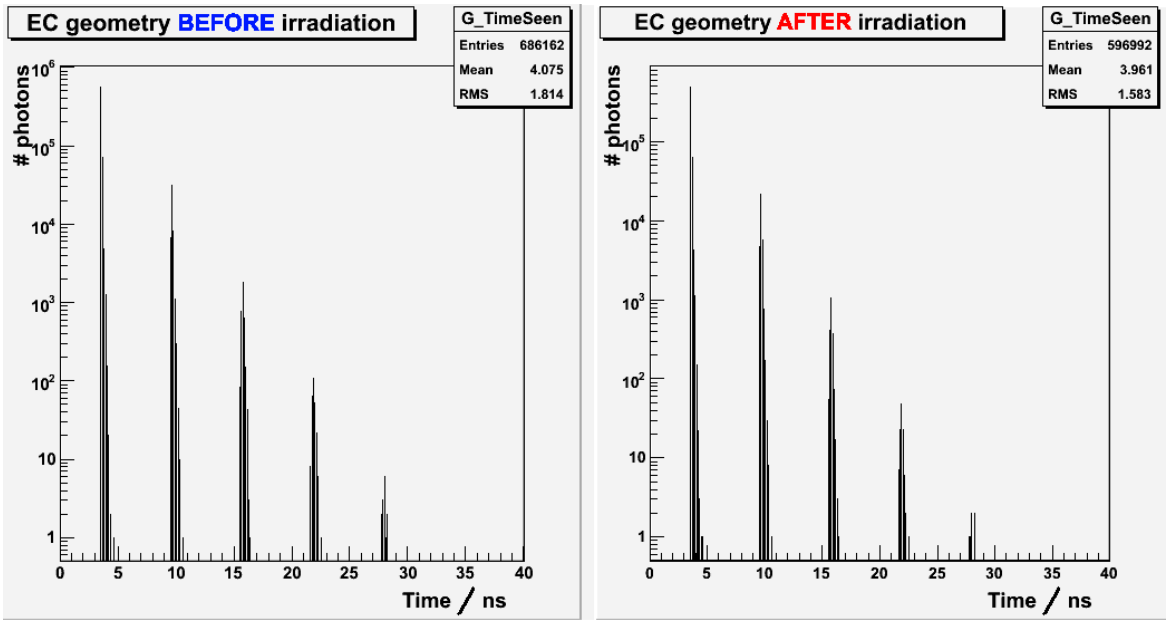

Figure 3.11: The figure shows the travel time of the photons between light source and detector in a crystal before and after irradiation. In the right picture, the amount of arriving photons is decreased due to the radiation induced absorption.

3.2.2 Transversal transmission and non-uniformity

The transverse transmission which is not measured at Gießen, provides a qualitative statement concerning the homogeneity of the crystals. The measurements of this property by the ACCOS machine are in principle quite similar to the longitudinal measurements. A separate photospectrometer, also using a large area photodiode as detector, measures the transverse transmission at the same wavelengths perpendicular to the long axis (every 4 cm) like for the longitudinal measurement (Fig. 3.12). The relevant parameter is the maximum deviation of the wavelength $\Delta\lambda$ where the curve passes the 50% limit and is defined as

$$\Delta\lambda \quad = \quad \lambda_{\max} - \lambda_{\min}. \tag{3.5}$$

As already mentioned, the absorption edge is very sensitive to any defects and concentration of doping. A relatively big $\Delta\lambda$ is a hint for a non-uniform crystal along the crystal axis. Therefore, this parameter should not exceed a value of 3 nm.

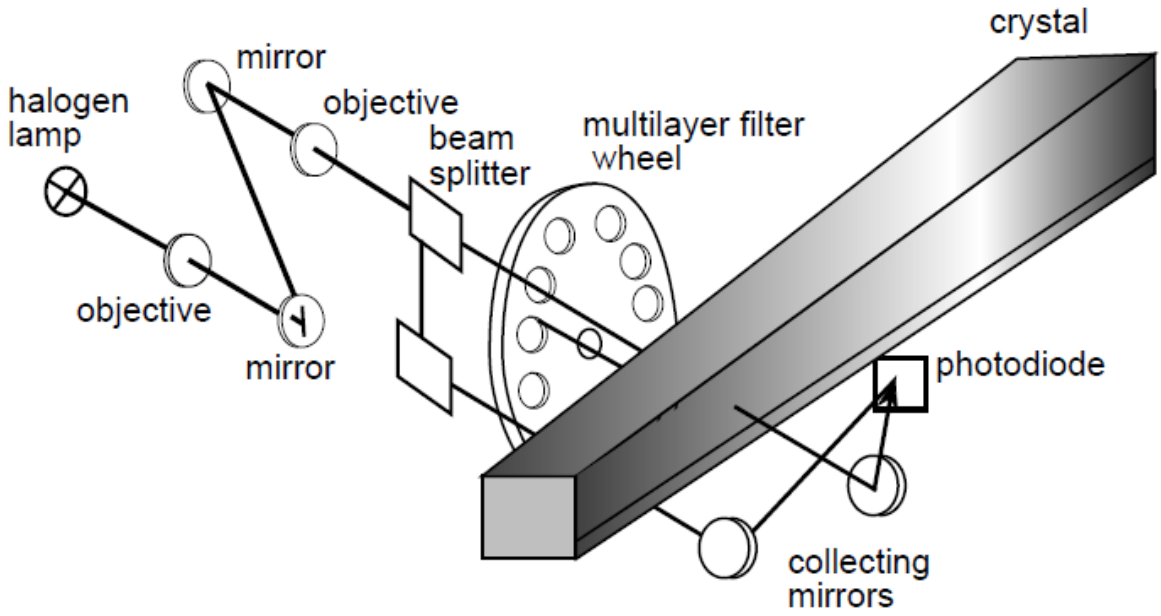

Figure 3.12: Arrangement of transversal transmission measurements with the ACCOS machine [ACC1].

3.3 Light yield

The LY is an important parameter for the contribution to the stochastic term of energy resolution of the calorimeter and is usually expressed in photoelectrons per MeV. As described in the previous chapters a gain factor of almost 8 was achieved by quality improvement and by additionally cooling down the crystals to $-25°C$ in contrast to the ECAL of CMS. It is reasonable to test every crystal at room temperature ($+18°C$) due to the shown correlation in section 2.3. These measurements are done by BTCP and CERN, but CERN only provides relative measurements which have to be calibrated. The light collection and therefore also the calibration strongly depend on the geometry. A stronger tapered crystal has a higher LY because of the focusing effect which is in that case more effective. For that reason, the absolute calibration in Gießen has to be done for each geometry. An investigation concerning LY collection depending on the geometry by simulations is described in section 3.3.3.

3.3.1 Setup for measurements at CERN and BTCP

Both facilities are exploiting the method of delayed coincidences to measure scintillation kinetics and scintillation LY [CMS7]. The measurements take place in a dark room to avoid the influence of any spurious light source since the crystals are not covered

by a reflector foil or wrapped to be light tight. As consequence, only totally reflected scintillation light will be collected. A ^{22}Na source is used which is a β^+ emitter. The arrangement of the delayed coincidence method is schematically shown in Fig. 3.13. One of the two 511 keV photons of the annihilation process is detected by a BaF_2

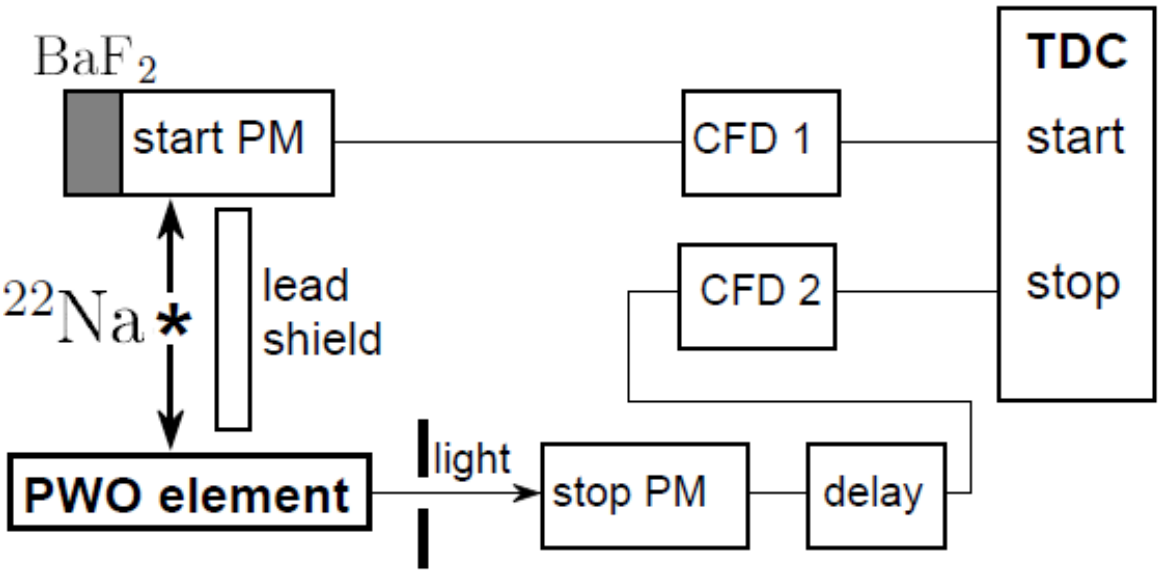

Figure 3.13: Configuration of the delayed coincidence method to measure kinetics and scintillation LY of the samples. The source is moveable along the crystal [ACC1].

crystal which has a more than one order of magnitude higher LY compared to PWO [NOV1]. This signal triggers the DAQ for reducing the background and generates a time marker of the excitation in a start-channel, while the second coincident photon excites scintillation in the lead tungstate crystal which will generate the stop channel. The timing uncertainty is of the order of a few 100 ps mostly caused from electronic components (PMT, CFD[4], TDC[5]). Additionally, to reduce random coincidences the activity of the source should not exceed 10^5 Bq.

3.3.2 Light yield calibration

Due to the measurement procedure of comparing the samples with reference crystals, the quality test station at CERN only provides LY measurements which have relative units. These values have to be calibrated with a calibration coefficient C to get the

[4]CFD = Constant Fraction Discriminator
[5]TDC = Time to Digital Converter

usual unit phe/MeV. This is done in Gießen.

$$\mathrm{LY}_{\mathrm{Gießen}}[\mathrm{phe/MeV}] \quad = C \cdot \mathrm{LY}_{\mathrm{CERN}}[\mathrm{a.u.}] \tag{3.6}$$

The measurements for absolute calibration of the LY is quite different from the procedure of measuring at CERN but it comes closer to the final readout in the $\overline{\mathrm{P}}$ANDA experiment. Fig. 3.14 shows the setup which was used for the measurements. The crystals are wrapped with 5 layers of teflon-foil and an aluminium-foil to optimize light collection by a reflective surface. The scintillation light is initiated by photons of 662 keV energy of a ^{137}Cs source. ^{60}Co and ^{22}Na sources can not be used since some crystals are contaminated with α-emitters which produce background signals corresponding to $1.2 - 1.4$ MeV photon energy. The readout is the task of a standard photomultiplier (PMT) with fused silica window and bialkali photocathode (Hamamatsu R2059, QE(420 nm) $\approx 20\%$). The photomultiplier signal is integrated over time ranges of 1 μs and 100 ns, respectively, and the photopeak is fitted with a Gaussian. The pedestal and single electron peak (SEP) are determined, which are required to

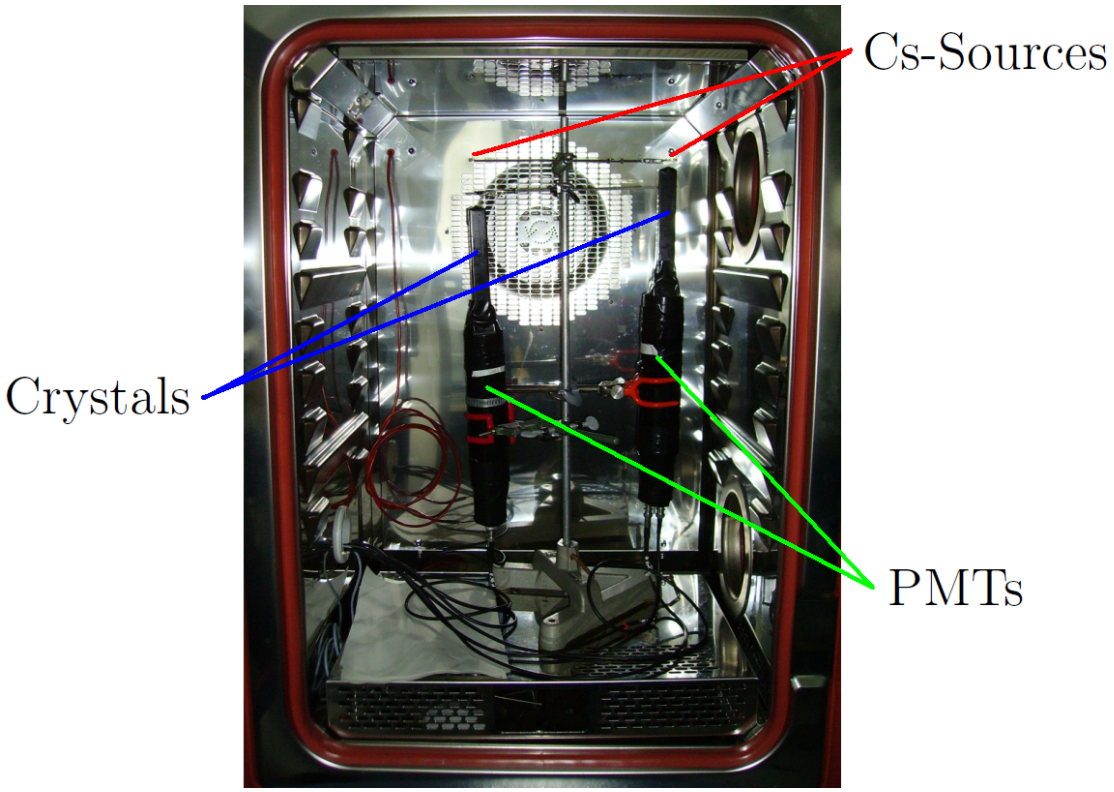

Figure 3.14: The picture shows the setup which is used for the LY calibration measurements in Gießen. It is mounted in a fridge to keep the temperature constant at $T = 18°\mathrm{C}$ and also to perform measurements at $T = -25°\mathrm{C}$.

deduce the LY according to the following equation:

$$\text{LY [phe/MeV]} = \frac{pp_{\text{Crystal}} - pp_{\text{Pedestal}}}{pp_{\text{SEP}} - pp_{\text{Pedestal}}} \cdot \frac{1}{E_\gamma} \tag{3.7}$$

The deduced LY is not corrected for the limited quantum efficiency of the phototube. Measurements were performed for two geometries: EC and Type 1. Only these two geometries were delivered in the first two lots and the results for their calibrations are shown in Fig. 3.15.

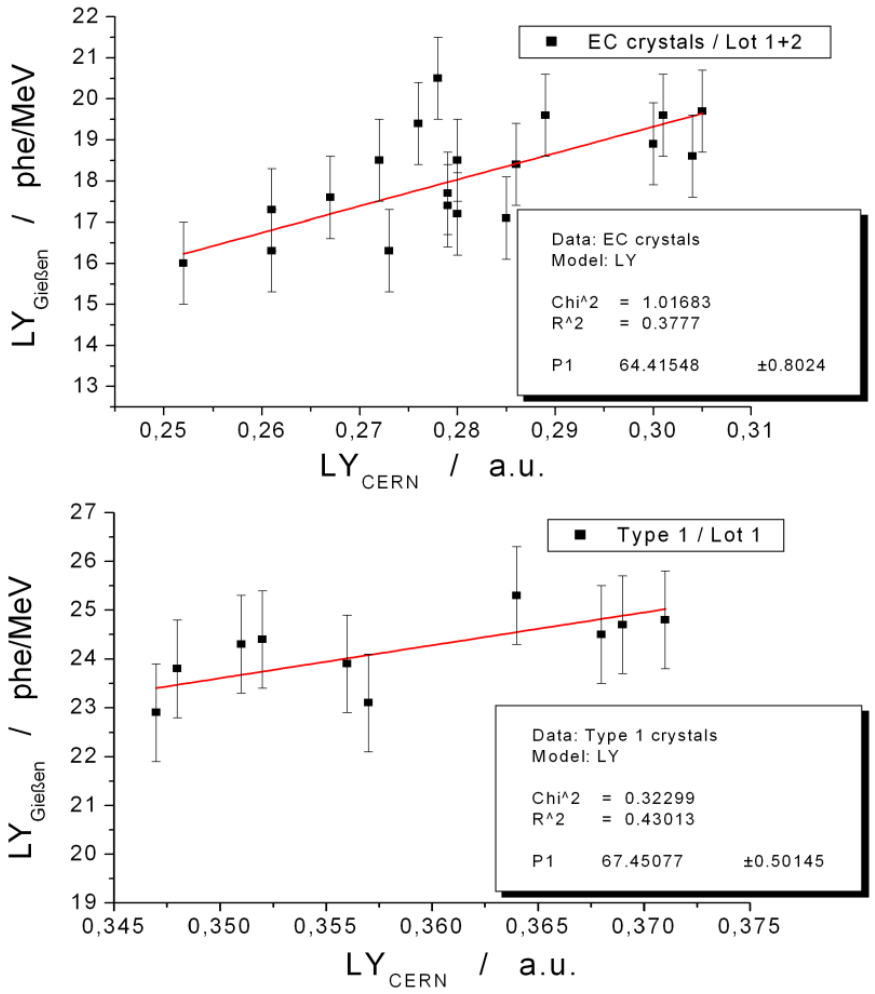

Figure 3.15: The upper and lower picture shows the result for the calibration of the EC and the type 1 crystals respectively. For each lot and each geometry 10 randomly chosen crystals were measured. The error of 1 phe/MeV is based on experience and mainly due to the non perfect coupling of crystals to the PMT window.

3.3.3 Studies of light collection depending on the geometry

First analyses concerning the light yield distributions of lot 1 (only type 1 and EC crystals) show a significant difference due to the more pronounced focusing effect of the type 1 geometry which is the most tapered geometry (compare Fig. 3.2). Simulations are performed to reproduce this geometrical effect.
Starting from the previously described simulations (3.2.1.3) some further assumptions were included to have a more realistic environment for these studies. Lead tungstate is taken as a negative uniaxial birefringent system with two different indices of refraction depending on the direction, displayed in Fig. 3.16 [BAC]. The index of refraction is usually inserted to LITRANI by the so called "Sellmeier law":

$$n(\lambda) \quad = \quad \sqrt{1 + A^2 + \frac{B^2\lambda^2}{\lambda^2 - C^2}} \tag{3.8}$$

This law describes the asymptotic behaviour of the index in the relevant wavelength region originating from the oscillation of atoms forced by an electromagnetic wave. For the generation of scintillation light with a radioactive source the photo effect cross

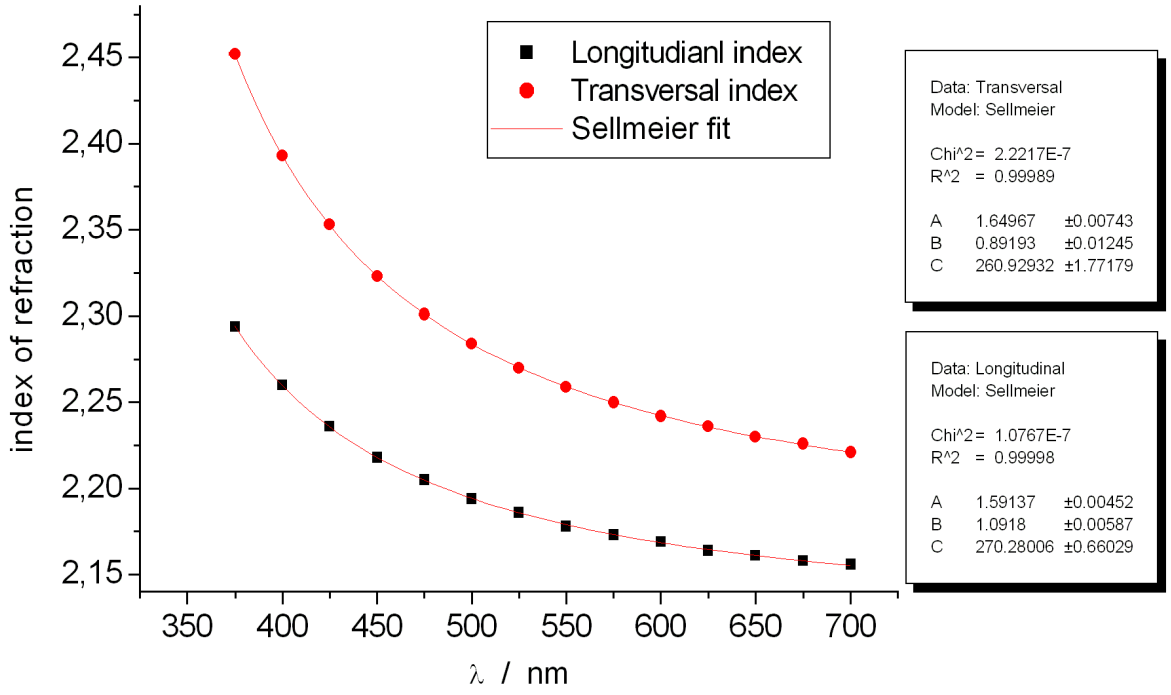

Figure 3.16: The points of the plot show the given values for the indices of refraction in both directions. The fit parameters which are listed on the right are used for the simulations of light collection to generate automatically the indices of refraction with 3.8.

section for lead tungstate has been implemented. Values in the relevant energy range

can be looked up in a database [DBCS] and are stored in two arrays as discrete points. LITRANI itself then generates a continuous spectrum with spline[6] fits between the data points. Charge and mass numbers have to be inserted into the simulation for using a Compton scattering algorithm, presented in [COMP]. The described fit proceeding for the photo effect is also used for the implementation of the QE of the PMT which is supported by a data sheet of the Hamamatsu company [HAM].
The new setup which is used for these simulations is shown in Fig. 3.17 and should come as close as possible to the described one presented in Fig. 3.14. In LITRANI it is possible to define any kind of wrapping to increase the light collection and therefore the number of converted photoelectrons. The wrapping is represented by an aluminium foil but without an additional coating of teflon. Like in the measurements for the LY

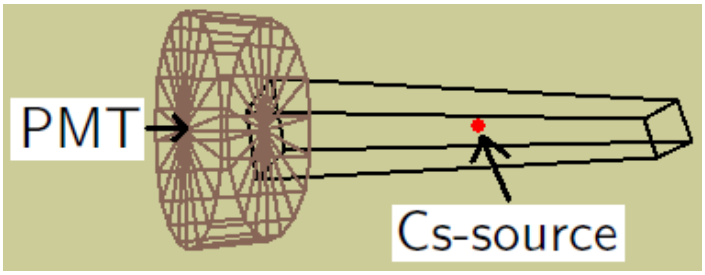

Figure 3.17: Inserted setup for the investigation of the light collection depending on the position of the radioactive source which is moveable along the crystal axis.

calibration a Cesium source was used with a γ-energy of 662 keV which emits photons isotropically. In contrast to the real experiment the source is placed inside the crystal, starting in the center of the small end face and then successively shifted forwards the large end face in steps of 2 cm along the axis of the crystal. At each position a fixed number of γ's is generated and the ratio between detected and generated photons (efficiency) which originate from the scintillation process is recorded. Only the main scintillation component of lead tungstate at 420 nm is included with a standard deviation of 40 nm and a decay time of 10 ns. The results of two different geometries (type 1 and EC) in terms of the efficiency (ratio between detected and generated photons) are shown in Fig. 3.18. Especially the shape of the curves are very well comparable to investigations (similar device as described in 3.3.1) which where performed by the EMC group at the Uppsala university and presented at a $\overline{\text{P}}$ANDA meeting [MM]. Fig. 3.18 shows the results as a function of the distance of the source to the PMT. The slope is different but this was expected due to the different focusing effect for both geometries. Another point which is a little bit questionable is the size of the absolute numbers. For γ's with the mentioned energies and an absorption length of a few cm the efficiency given by the simulations is around 5.5 and 4.0% for Barrel and EC crystals respectively. These low numbers are due to the defined contact be-

[6] piecewise defined function by polynomials

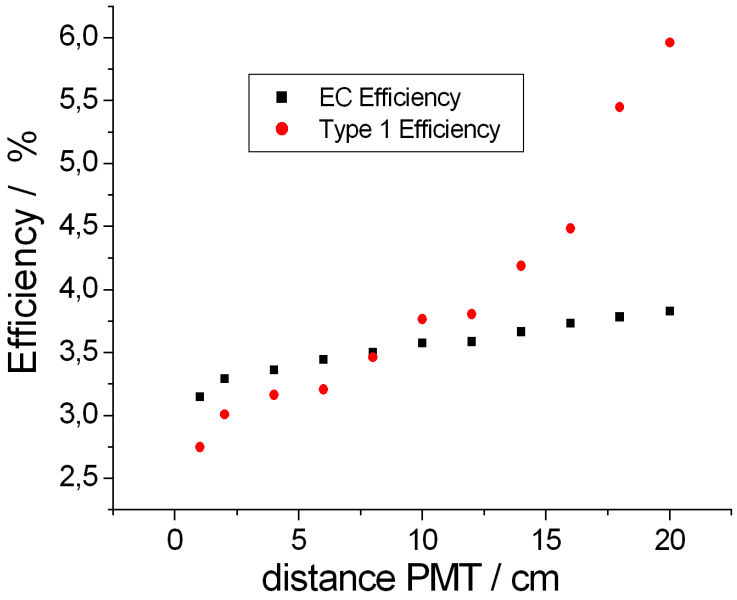

Figure 3.18: Simulation results for the investigation of light collection. The figure shows the detection efficiency depending on the distance between γ-source and PMT.

tween PMT and crystal. In contrast to the real measurements for the LY calibration where one expects around 10%, no optical coupling (e.g special grease) was included. The difference of the indizes of refraction of the entrance window (made of sodocal, $n(420\text{ nm}) = 1.535$) and the lead tungstate crystal are the reason for the light loss because of totally reflected photons.
The results presented in Fig. 3.18 will be picked up and further discussed in Sec. 4.2.4.

3.4 Scintillation kinetics

The scintillation kinetics describes the change of scintillation LY within a certain time after excitation. Parameters of the scintillation kinetics can be presented as decay times of the scintillation light components or as number of scintillation photons emitted in specified gates. For mass quality inspection, the ratio LY(100 ns)/LY(1 μs) was chosen to judge whether a crystal has sufficient fast kinetics or not. The LY is measured with integration gates of 100 ns and 1 μs respectively to calculate the ratio. This property is not expected to become problematic with a specification of LY(100 ns)/LY(1 μs) $\geq$ 90% at T= +18°C. For a selected group of lot 3 it was also confirmed at Gießen that this ratio looks better (Fig. 3.19) and is even above the specifications at T= −25°C. That is the reason why this property is not further analysed in the final analysis. Fig. 3.20 shows a typical picture for presenting the scintillation kinetics of lead tungstate at different temperatures.

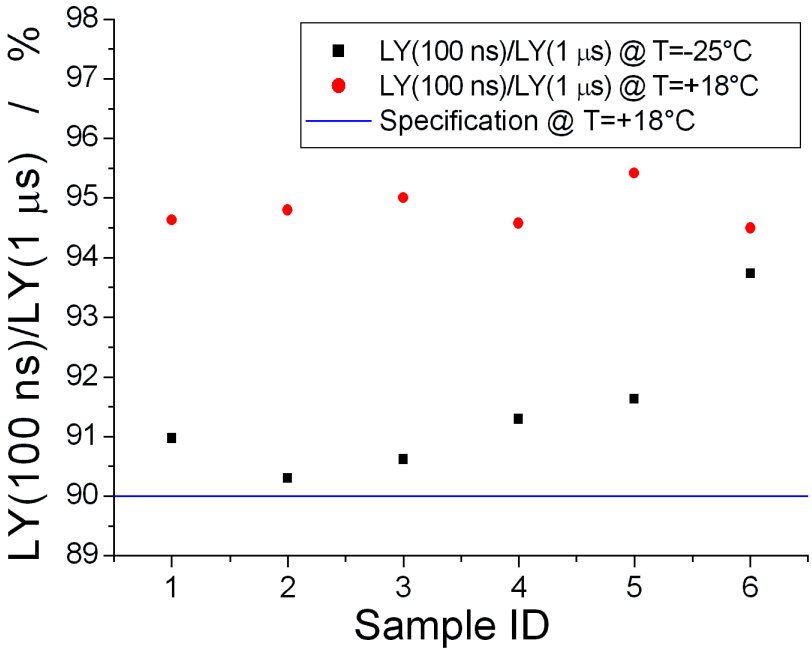

Figure 3.19: Measurements of the LY ratio between 100 ns and 1 μs at T= +18°C and T= −25°C, respectively.

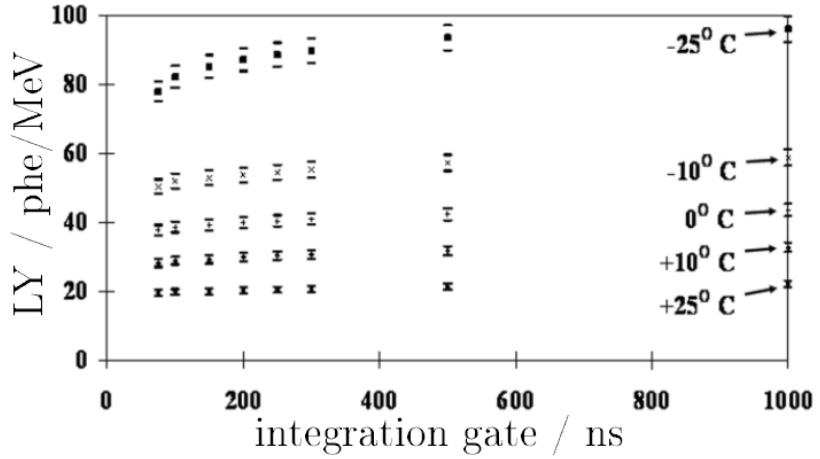

Figure 3.20: Typical collecting behaviour depending on the integration gate. In addition, one can see nicely the gain factor of 4 at −25°C with respect to +25°C [TDR].

3.5 Radiation hardness

The uniformity of the parameters of the scintillation material in a radiation environment is one of the most important properties to build an electromagnetic calorimeter with sufficient energy resolution. The scintillation mechanism itself is not affected by irradiation but the optical transmission in the relevant spectral region. This loss of transmission originates from color centers which are cause absorption bands and is expressed by the change of the absorption coefficient based on a pure exponential behaviour of the transmission as a function of crystal length d (in our case 20 cm).

$$\begin{aligned} \Delta k &= k_{\text{after}} - k_{\text{before}} \\ &= \frac{1}{d} \ln \left(\frac{T_{\text{before}}}{T_{\text{after}}} \right) \end{aligned} \tag{3.9}$$

Fig. 3.21 shows the typical shape Δk for three crystals of different quality concerning the radiation hardness after irradiation with an integral dose of 30 Gy. The radiation hardness of the crystals with respect to specifications is tested at BTCP and also in Gießen. Both radiation facilities and the procedure of investigation will be presented in the following section.

3.5.1 Irradiation facility and test procedure at BTCP

The irradiation facility at BTCP was installed for the mass production for the CMS detector with technical assistance of RINP[7]. Fig. 3.22 shows the irradiation facility

[7]RINP = Research Institute for Nuclear Problems of Belarusian State University

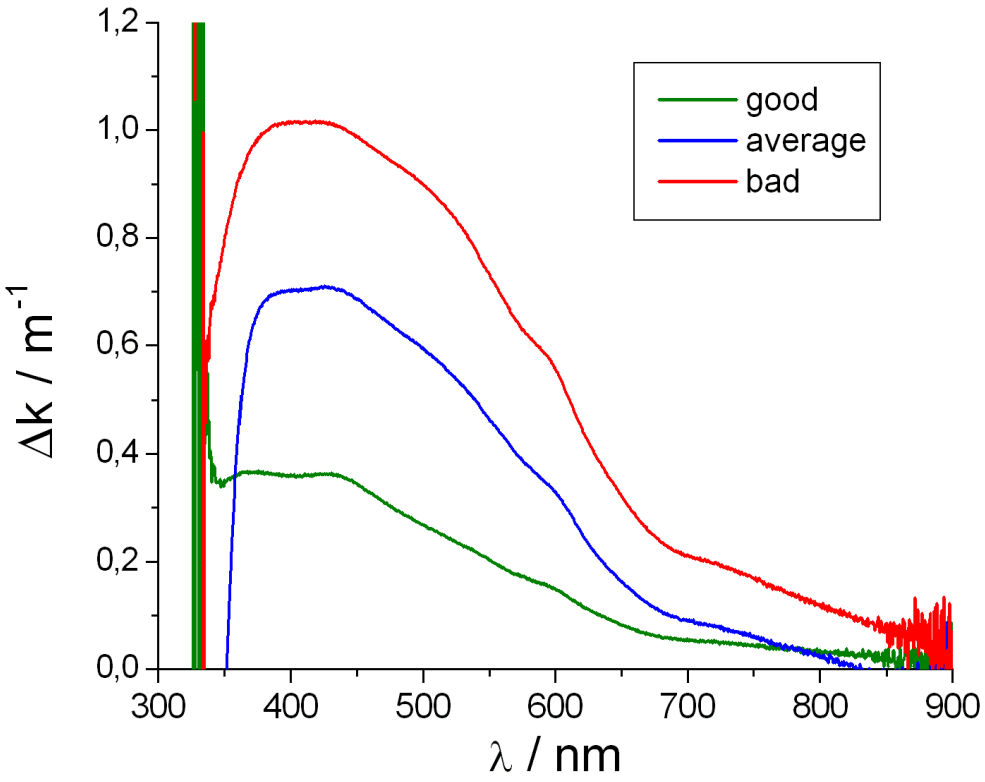

Figure 3.21: A typical Δk-spectrum of three crystals with different quality concerning the radiation hardness measured in Gießen. The maximum change of the absorption coefficient is around 400 nm and the slightly visible structures at 440 and 600 nm are indications for narrow absorption bands.

(left) the spectrometric setup (right). This setup is called RGB System according to the inspected wavelengths at 420 nm (blue), 570 nm (green) and 650 nm (red). For radiation protection, the used ^{60}Co with a dose rate of 1200 Gy/h is placed in a well for lateral irradiation. The equipment is able to measure four crystals in one cycle which takes about 7 minutes for irradiation and the optical measurements before and after irradiation.

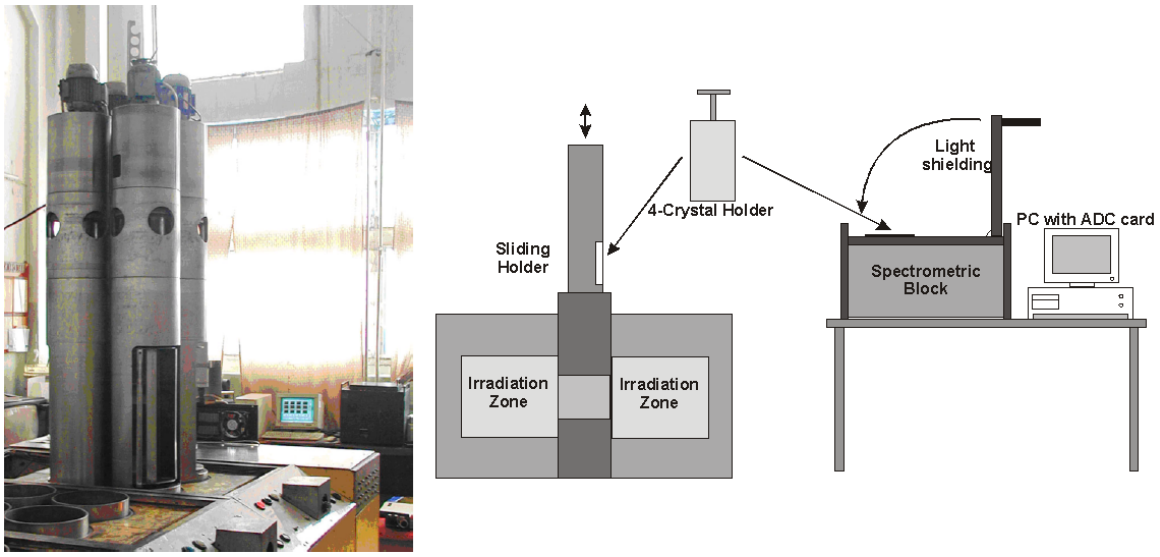

Figure 3.22: Left: The irradiation facility operating at BTCP in Russia. Right: Schematic layout of the arrangement for irradiation and spectrometric setup [TDR].

3.5.2 Irradiation facility and test procedure at Gießen

The irradiation facility at the Strahlenzentrum in Gießen is based on a set of several ^{60}Co sources (Fig. 3.23, left). For the irradiation of the crystals a moveable compartment is used which is shown in Fig. 3.23 (right). This compartment has at present a dose rate of about 3.3 Gy/min and is sufficiently homogeneously distributed over the whole area. This was verified by KHG[8] by analysing 5 flat dosimeters. The positions of these dosimeters in the compartment and the results obtained for the dose rate after an irradiation time of 140 minutes are shown in Fig. 3.24. During the measurements of the first crystals, it turns out that Δk strongly depends on the time when the crystals are remeasured after irradiation. This fact is due to fast recovery components which were further investigated at room temperature and can be seen in Fig. 3.25. This was the reason why the group in Gießen decided to measure the transmission for all future

[8]KHG = Kerntechnische Hilfedienst GmbH

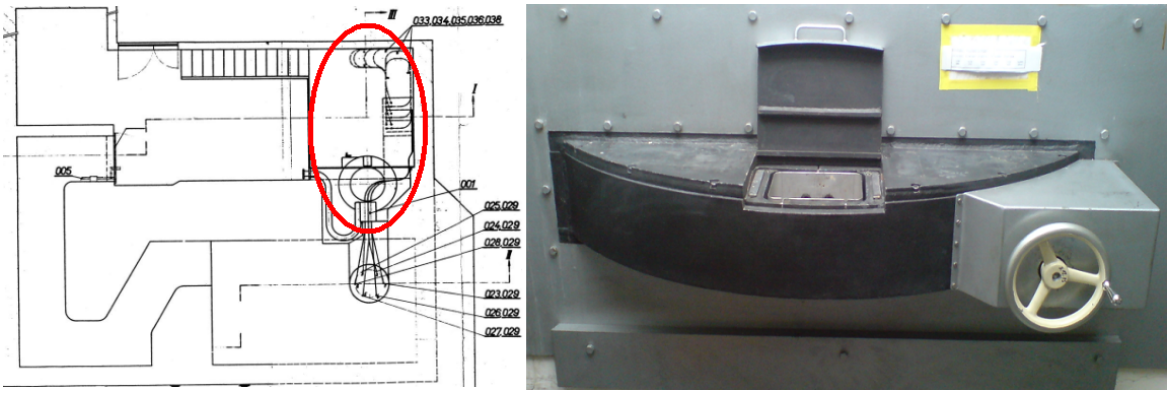

Figure 3.23: Left: Ground plan of the irradiation facility at the Gießen Strahlenzentrum. The place where the crystals were measured and irradiated is encircled in red. Right: A picture of the moveable compartement.

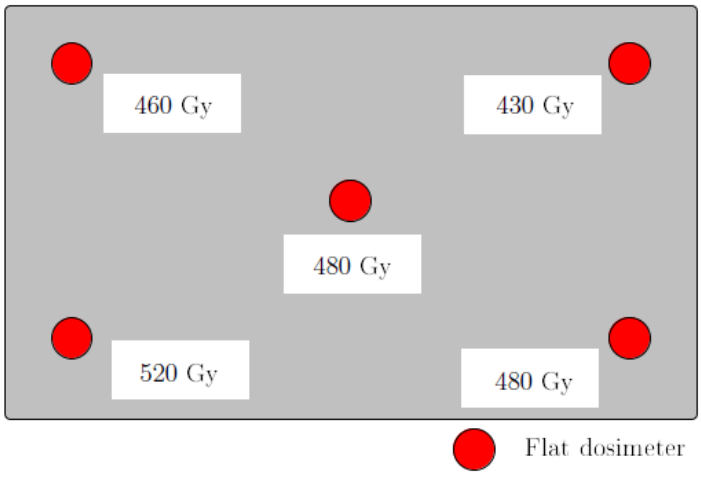

Figure 3.24: Schematic top view of the moveable compartment (Fig. 3.23). One can see the red dots which stand for the observed positions where the dosimeters were placed and the obtained results. The obtained average dose of 500 Gy fits to the dose rate of 3.6 Gy/min at that time and the irradiation time (140 minutes).

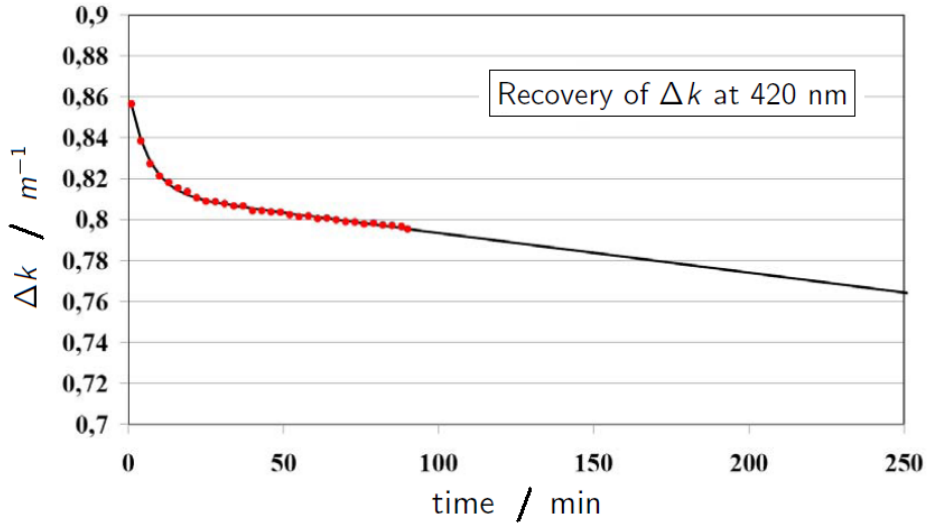

Figure 3.25: Recovery of a PWO crystal depending on the time after irradiation at room temperature. Some relatively fast recovery components become visible within the first approx. 20 minutes [VD].

tests 30 minutes after irradiation to minimize uncertainties. This condition has been defined in an addendum to the contract before. During this time, the crystals have to be kept light tight to avoid stimulated recovery. These measurements are the task of the described spectrometer in Fig. 3.6 which was installed at the Strahlenzentrum to avoid any unnecessary moving of the crystals.
Another problem which came up during the first period of measurement was the approaching rejection deadline. Therefore whole measurement routine had to speeded up. Due to an existing correlation between the Δk data of BTCP and Gießen (Fig. 3.26) it was decided to measure at first only crystals which exceed a critical value $\Delta k_{BTCP} > 0.7\ m^{-1}$. It is clear that after the decision of rejection the remaining crystals have to be measured to get the complete distribution of Δk and to find the radiation hardest crystal for the FEC.
Several kinds of errors have to be taken into account in the final analysis. At first the transmission measurements has an absolute error of 0.4% for the transmission at 420 nm (see 3.2.1.2). The impact on the Δk can be calculated by

$$\begin{aligned} \Delta(\Delta k) &= \sqrt{\left(\frac{\partial(\Delta k)}{\partial T_B}\Delta T_B\right)^2 + \left(\frac{\partial(\Delta k)}{\partial T_A}\Delta T_A\right)^2} \\ &= \frac{1}{0.2\ \mathrm{m}}\sqrt{\left(\frac{\Delta T_B}{T_B}\right)^2 + \left(\frac{\Delta T_A}{T_A}\right)^2}. \end{aligned} \tag{3.10}$$

With ordinary values for ΔT_B and ΔT_A and in addition $\Delta T_B = \Delta T_A = 0.4\%$ one obtains a relative error of $\sim 4\%$. Also the delay time after irradiation contributes

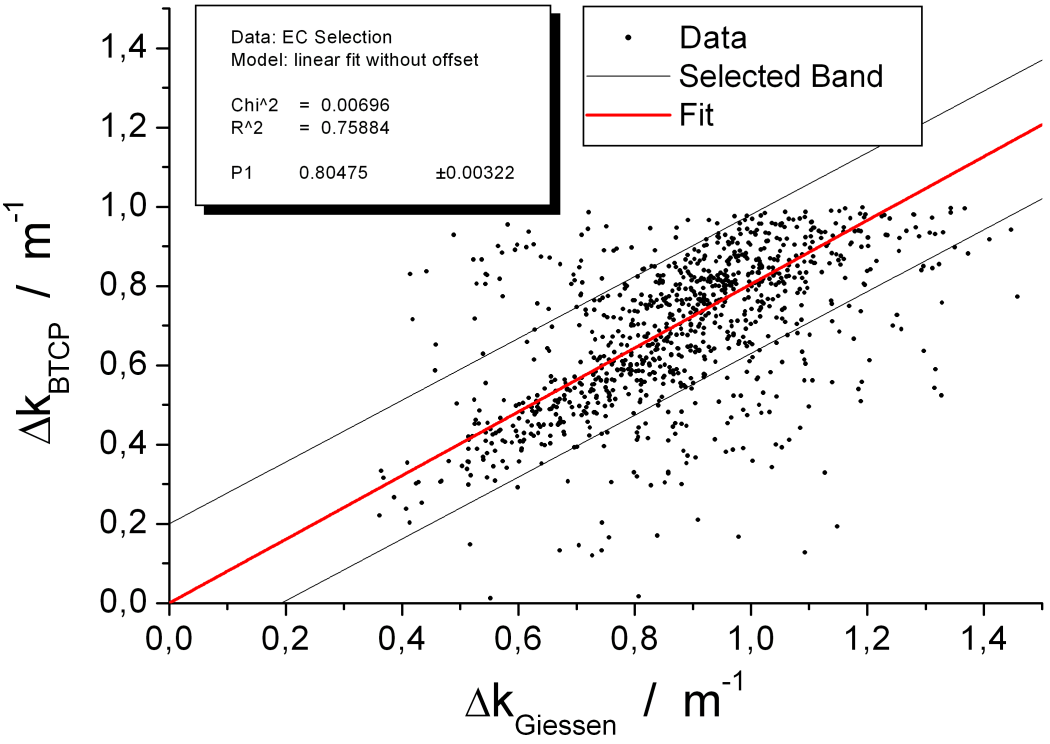

Figure 3.26: Correlation of Δk for EC crystals between BTCP and Gießen to speed up the measurements. All crystals were measured 30 minutes after irradiation. Among the clear correlation, also a not negligible amount of data deviates which is not explainable. Because of the strict cut at 1.0 m^{-1} in case of the BTCP data, only the points within the marked region (black lines) were used for the linear fit.

to the error bars because of the recovery process. But a variation of the start of measurements of a couple of minutes after irradiation can be estimated to be below 1%.
Another systematic error is caused by multiply reflected photons. The simulations introduced in 3.2.1.3 give an overall fraction of 2% of photons which pass the crystal twice and more. The formula for calculating Δk takes in principle only photons into account which pass the crystal only once. This can be estimated from the difference considering multiple reflections or not.

$$\Delta k_{\text{with MR}} = \frac{1}{d} \ln \left(\frac{\mathrm{T}_{\text{One/before}} + \mathrm{T}_{\text{Rest/before}}}{\mathrm{T}_{\text{One/after}} + \mathrm{T}_{\text{Rest/after}}} \right) \tag{3.11}$$

and

$$\Delta k_{\text{without MR}} = \frac{1}{d} \ln \left(\frac{\mathrm{T}_{\text{One/before}}}{\mathrm{T}_{\text{One/after}}} \right) \tag{3.12}$$

with

MR	:	Multiple Reflection
$\mathrm{T}_{\text{One/before or after}}$	:	Photons which pass once trough the crystal
$\mathrm{T}_{\text{Rest/before or after}}$	:	Photons which pass twice and more trough the crystal.

As it was mentioned the absorption length, which is one of the input parameters for the simulation, was calculated by Eq. 3.4 from the experimental transmission data. Fig 3.27 shows the procedure for calculating the error on Δk due to multiple reflection. This routine was repeated for several crystals of different quality considering

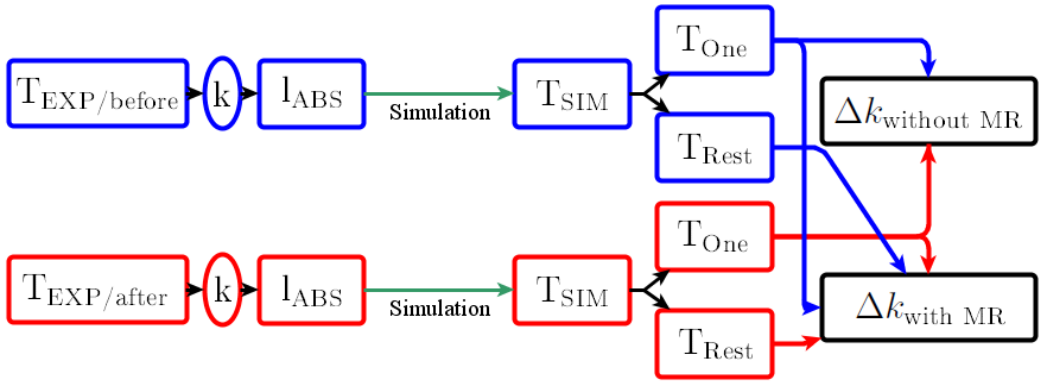

Figure 3.27: Procedure for calculating the error on Δk due to multiple reflection. The blue and red frames stand for before and after irradiation, respectively. T_{One} and T_{Rest} were determined by integrating the corresponding peaks in Fig. 3.11 which shows the result of one simulation run.

the transmittance before irradiation. The relative error

$$\frac{\Delta k_{\text{with MR}} - \Delta k_{\text{without MR}}}{\Delta k_{\text{without MR}}}$$

varied over a range of 1.5%-3.7%. These values are in agreement to the theoretical prediction.
In order to en sure that all mentioned errors are covered, the acceptable limit for the Δk was changed. Also the different delays after irradiation for the very first measurements have to be taken into account due to the stronger influence by the recovery process. Tab. 3.3 shows the amount of crystals with the modified specification limit depending on the delay before the start of measurement.

Number of crystals	Delay after irradiation / min	modified specification / m^{-1}
60	5	1.15
80	20	1.15
1278	30	1.1

Table 3.3: Number of crystals with corresponding delay after irradiation and modified specification limit.

Chapter 4

Results of Quality Control

In the meantime the first two lots which comprise an amount of 1750 crystals (375 type 1 and 1375 EC geometry) passed all three quality stations and were completely analyzed. The analysis performed in this thesis represents an example for the whole quality inspection of the lead tungstate crystals. All measured data were included in a database (DB) for better and direct comparison of the obtained results. This chapter summarizes the achieved quality with respect to the specifications for the $\overline{\text{P}}$ANDA EMC and to the CMS quality for all relevant properties. Furthermore several correlations between the individual test stations will be discussed and emerging discrepancies analyzed.

4.1 Database management of the measured crystal properties

For each lot BTCP and CERN send a huge xls[1]-file to Gießen which contains all measured data. Also in Gießen all measurements for the transmission and the Δk-values are stored in a xls-file. One can imagine that it is quite laborious to do the analysis of the quality inspection by handling a bunch of different files. The following reasons were decisive to put all these data sheets in one DB and to program an interface for external users:

- overview of the huge amount of measurements
- fast access and download of selected data
- availability of online correlations between the testing facilities
- easy management and updating

[1] default format for a spreadsheet-application of Microsoft Excel

The password protected DB is created by PHPMYADMIN which is an open source tool written in PHP[2] and is able to handle the administration over the World Wide Web. The whole structure is based on the relational DB management system MySQL[3] [MySQL]. Altogether the DB consists of 5 tables which are listed in Tab. 4.1.

Table caption	Content
btcp	measured data from BTCP
cern	measured data from CERN
giessen	measured data from Gießen
comments	individual comments for a single crystal
gen_comments	general comments, like e.g. the import status of the DB

Table 4.1: Table content of the DB.

Another challenge was to program an interface of the described DB for users which are not allowed to perform administrative operations. This was realized by a program consisting of different script languages: PHP, HTML[4] (visualisation in a browser) and MySQL (interacting with the DB). The interface offers uncomplicated opportunities to produce online correlations, downloading selected data as txt-file or adding a single dataset to a list of Tab. 4.1. Two screenshots of the start screen and a produced online correlation between CERN and BTCP at 360 nm are shown in 4.1.

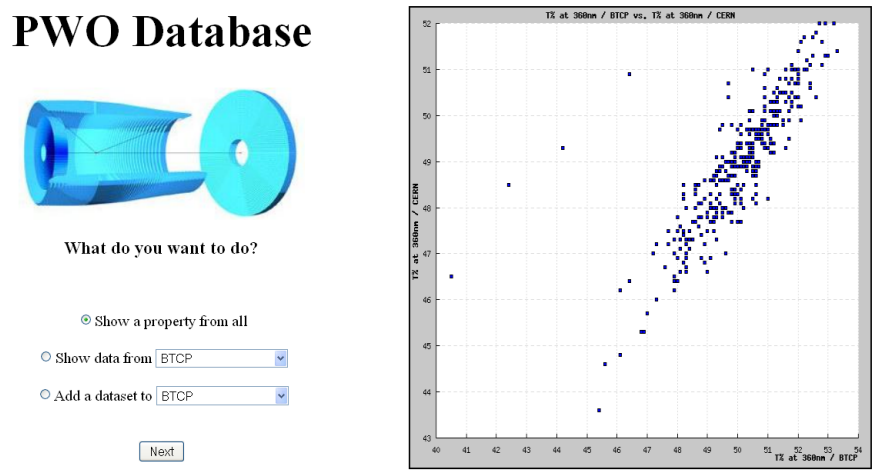

Figure 4.1: Left: Start screen DB interface. Right: Online correlation to get a first impression of the data distribution.

[2]PHP = Personal Home Page; scripting language originally designed for producing dynamic web pages
[3]MySQL = My Structured Query Language
[4]HTML = Hyper Text Mark-up Language

4.2 Results with respect to rejection

All parameters of the first two lots will be successively discussed and compared with the defined specifications of the contract for the crystals of the $\overline{\text{P}}$ANDA EMC. The majority of the distributions can be fitted with a Gaussian function. One can find a table with the listed fit parameters of all properties in appendix A.

4.2.1 Geometry

Fig. 4.2 and Fig. 4.3 show the measured geometry parameters with the TOPAZ 7 machine at BTCP and CERN respectively. On the x-axis the deviation between the desired size and the measured one is plotted. The labels of the single histograms are the captions of the individual edges of the crystal and can be looked up in Fig. 3.2.

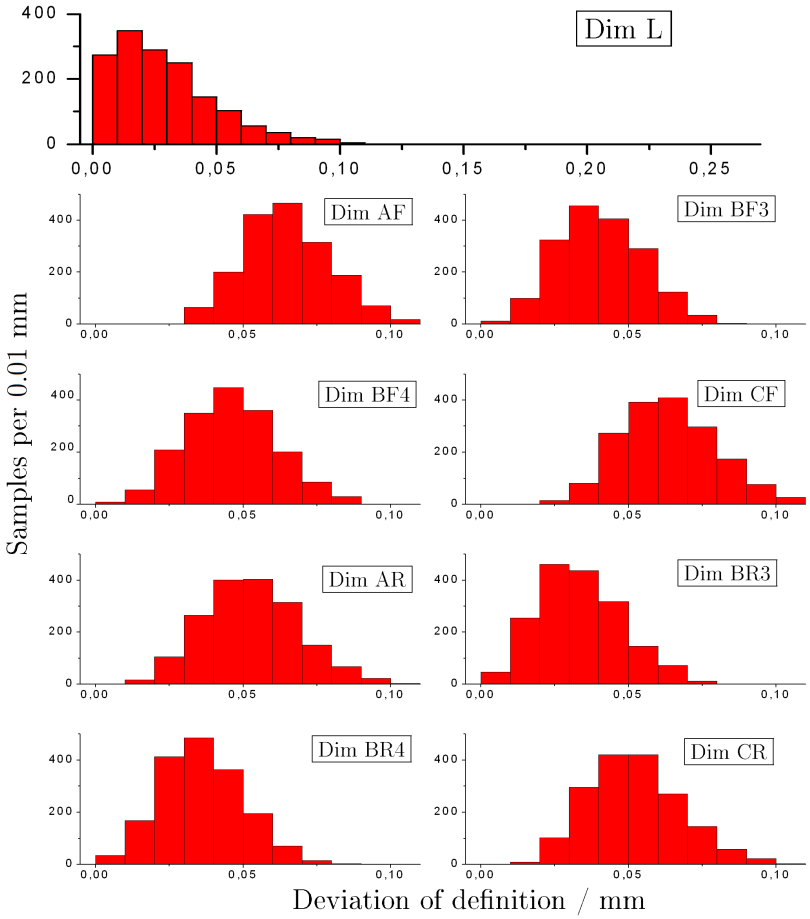

Figure 4.2: Geometry data - CERN.

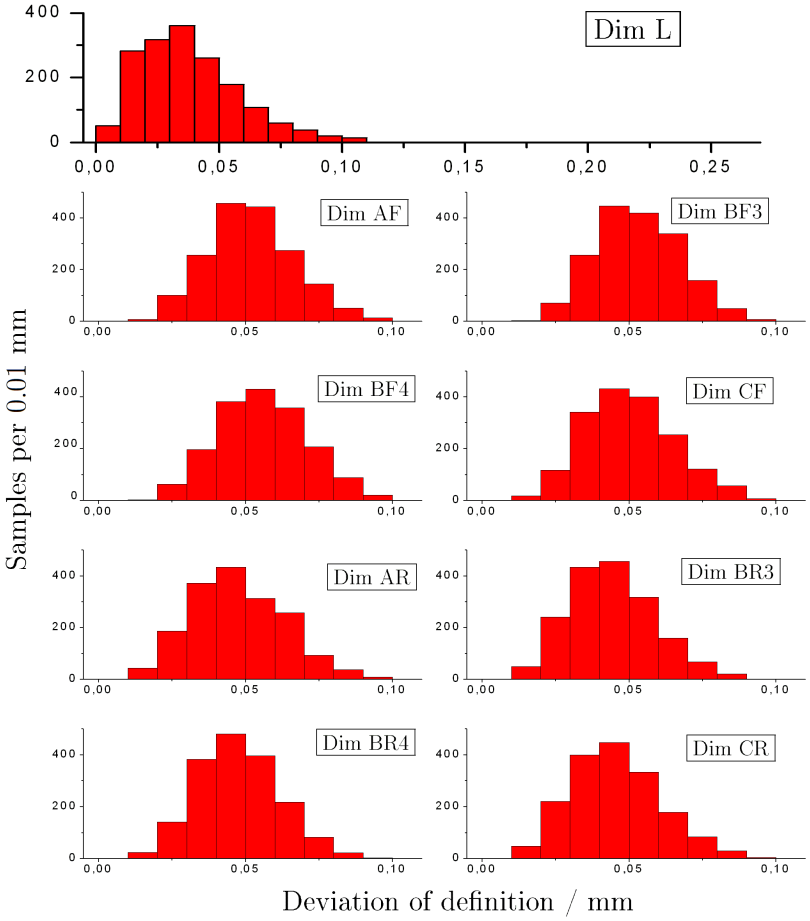

Figure 4.3: Geometry data - BTCP.

At first one can conclude that all measured geometries are smaller then the defined limit. All parameters are within the geometrical specification range of $0/-0.1$ mm. Only in the BTCP-data of the full length, 187 crystals are decreasingly distributed over a range from $0.11-0.29$ mm. This small deviation in the longitudinal size is tolerable and is not critical for the implementation into the carbon alveoles.

Conclusion concerning the geometry: No necessity for rejection.

4.2.2 Longitudinal transmission

All data for the first two lots for each facility and each relevant wavelength are summarized in Fig. 4.5 with a bin size of 0.5%. Due to the perpendicular entrance of the beam and the planarity of the end faces no substructure becomes visible for the different geometries. Only for the CERN data at 420 nm and 620 nm two shoulders on the left side of the distribution are present but obviously due to poor statistics. Furthermore it is noticeable that the distribution at 360 nm is continuously broader than the others. This is due the manufacturing variations leading to a variation on the absorption coefficient which strongly increases in that region and has therefore a larger impact. Fig. 4.4 shows the averaged transmission spectrum from 10 randomly chosen crystals with the corresponding absorption coefficient. Altogether one can conclude that the transmission parameter is non-problematic. All samples show a longitudinal transmission well above the specification limits.

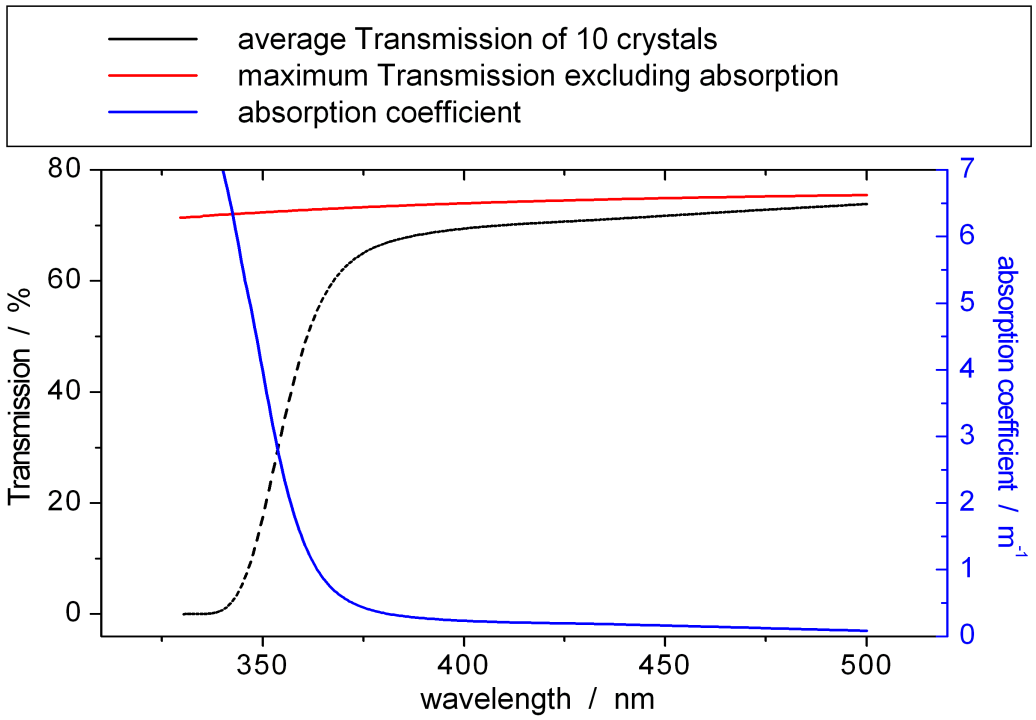

Figure 4.4: Averaged transmission spectrum of 10 samples and corresponding absorption coefficient. The red curve shows the theoretical maximum transmission based on multiple reflection [BAC].

Conclusion concerning the longitudinal transmission:
No necessity for rejection.

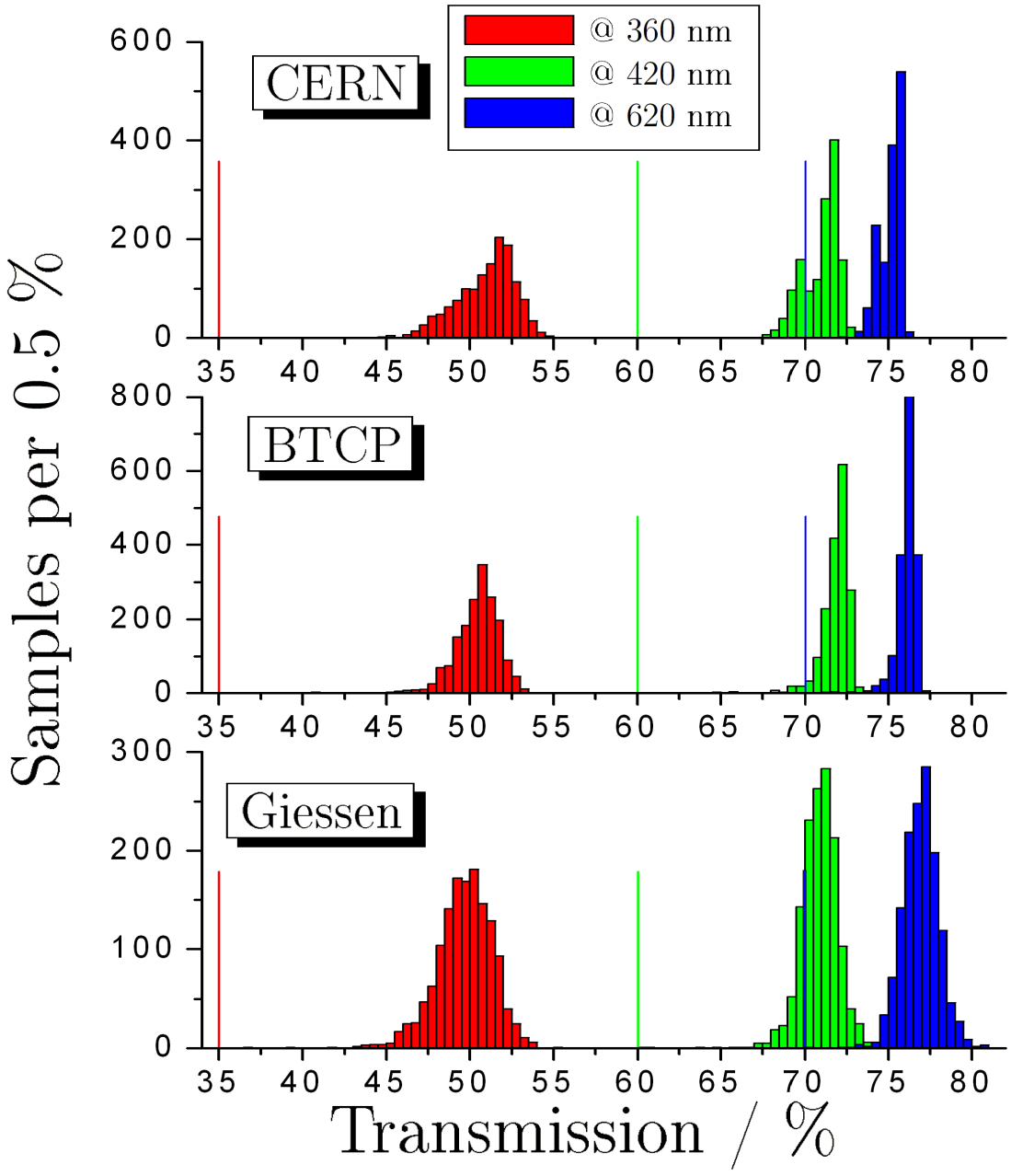

Figure 4.5: Longitudinal transmission data for all facilities including the specification limits marked as straight lines with corresponding color.

4.2.3 Transversal transmission

Fig. 4.6 shows the distributions of the $\Delta\lambda$ for both available geometries of BTCP and CERN. The data for the EC geometry looks quite comparable but the ones for the barrel type show a big discrepancy. The mean value of the CERN data is roughly two times larger than the one of the BTCP data. This fact will be further discussed in section 4.3. Nevertheless the data is far below the specification edge of 3 nm and is not expected to become serious for further lots. Altogether one can assume that the uniformity of the crystals along the full length is guaranteed.

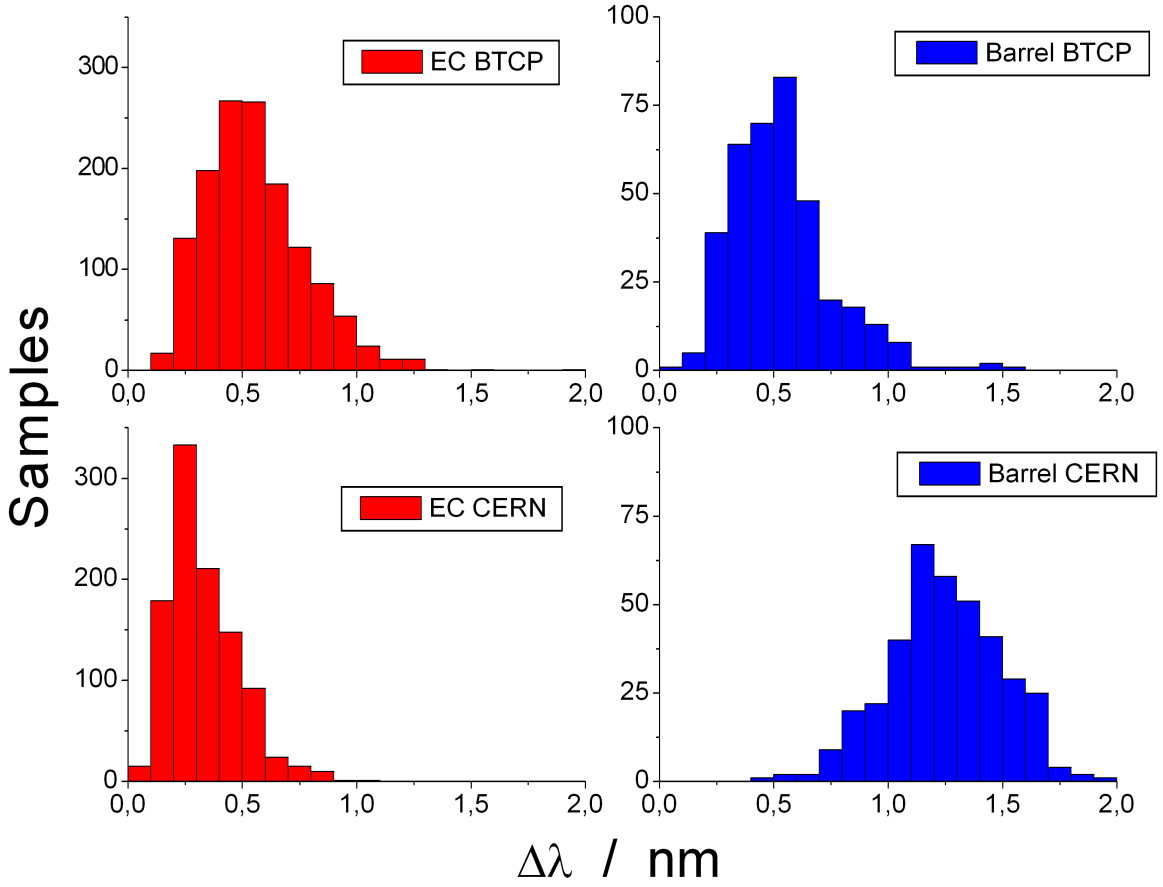

Figure 4.6: Transverse transmission data - BTCP and CERN. Concerning the transversal transmission and therefore also for the uniformity all crystals are acceptable. Only the deviation of barrel type crystals is an obvious hint for a systematic shift due to different ways of measuring.

Conclusion concerning the transversal transmission:
No necessity for rejection.

4.2.4 Light yield

The upper part of Fig. 4.7 displays the measured data for the LY by BTCP. The lower one shows the distribution of CERN with the calibration coefficients 64.42 phe/MeV for the EC and 67.45 phe/MeV for the type 1 geometry (compare Fig. 3.15). In case of the CERN data, all barrel type crystals show an excellent light yield with a mean value of approximately 25 phe/MeV. BTCP provides a value which is roughly one fourth less due to the different measuring procedure. For the EC geometry, however, both facilities obtain distributions with a comparable mean value of 18 phe/MeV. This means both procedures of measuring strongly depend on the geometry and therefore on the different levels of tapering. This fact will be further discussed in section 4.3. The significant differences between both geometries are still remarkable and were the initial motivation to perform the simulations with LITRANI, introduced in 3.3.3.
The result concerning the light collection efficiency depending on the position of a Cs-source in the crystal was already shown in Fig. 3.18. A photon emitted by a Cs-source is not able to make pair production due to its relatively low energy. To find out the energy distribution in a lead tungstate crystal one has to know the probability for photo effect and Compton scattering. These values ($\mu_{\text{Photo Effect}}$ and μ_{Compton}) at the relevant energy can be looked up in [DBCS]. The absorption length can be subsequently calculated by the following equation:

$$\begin{aligned} l_{\text{ABS}}^{662\text{ keV}} &= [\rho_{\text{PWO}} \cdot (\mu_{\text{Photo Effect}} + \mu_{\text{Compton}})]^{-1} \\ &= 2.589\text{ cm} \end{aligned} \tag{4.1}$$

This means roughly 80% of the incident photon energy is deposited within the first 4 cm and the generated scintillation light is collected according to the specific efficiency in that region. In order to normalize the simulation to the experimental results, the ratio between the relevant integrals of the efficiency ($\equiv \epsilon$) of both spectra in Fig. 3.18 were calculated.

$$\frac{\int_{16\text{ cm}}^{20\text{ cm}} \epsilon_{\text{Type 1}} dx}{\int_{16\text{ cm}}^{20\text{ cm}} \epsilon_{\text{EC}} dx} = 1.398 \tag{4.2}$$

This value is comparable to the ratio of mean values between barrel and EC crystals for the CERN data (Fig. 4.7).

$$\frac{< \text{LY}_{\text{Type 1}} >}{< \text{LY}_{\text{EC}} >} = 1.386 \tag{4.3}$$

Nevertheless, regarding the specification one can assume that all crystals show a sufficient LY. Only four EC crystals fall below the specification limit and have to be rejected.

Conclusion concerning the light yield: 4 EC crystals have to be rejected.

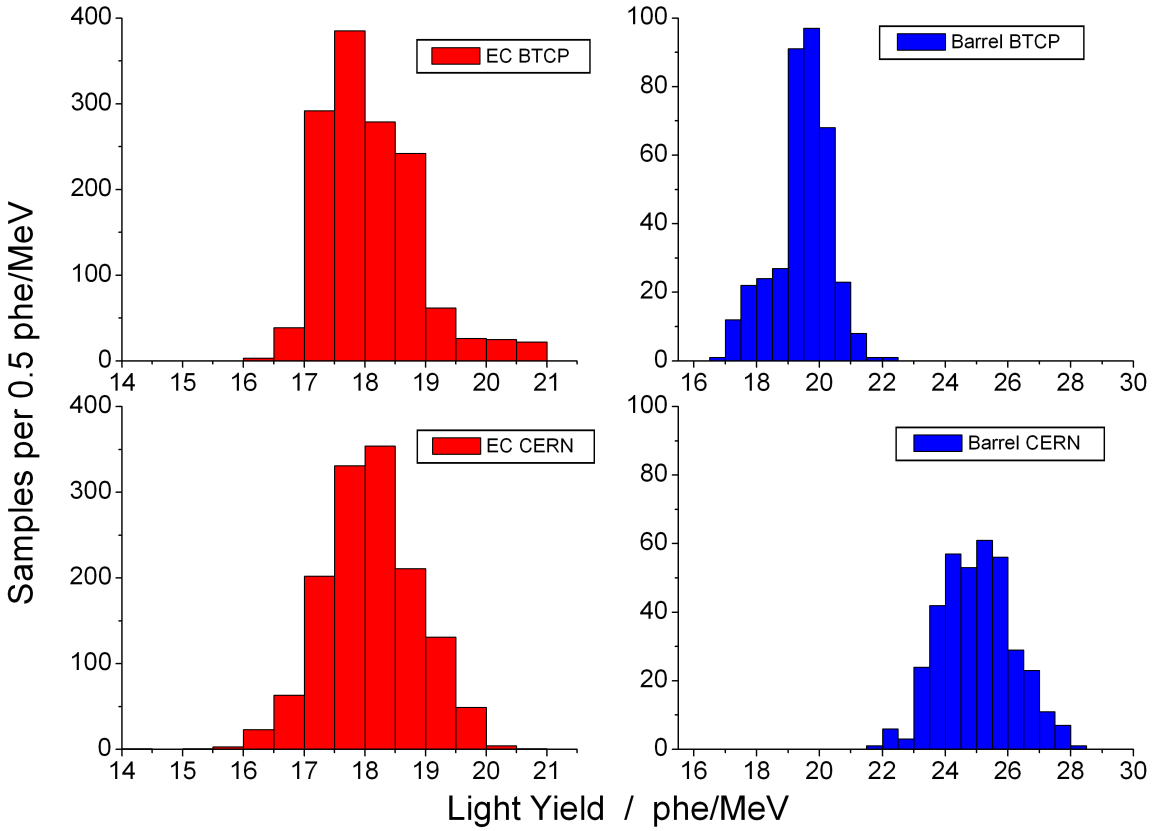

Figure 4.7: LY measurements from BTCP and CERN for both geometries. The difference between both geometries is attributed to the light collection efficiency depending on the distance between the origin of the scintillation light and the PMT.

4.2.5 Radiation hardness

The radiation hardness is the most critical property with respect to rejection. It is not necessary to make different plots for the geometry due to the planar end faces for all crystals. As it was mentioned in chapter 3.5.2, in the beginning the crystals were measured with different delays after irradiation. Fig. 4.8 shows the data from BTCP and Gießen distinguished by the delays including the modified specifications marked in grey.

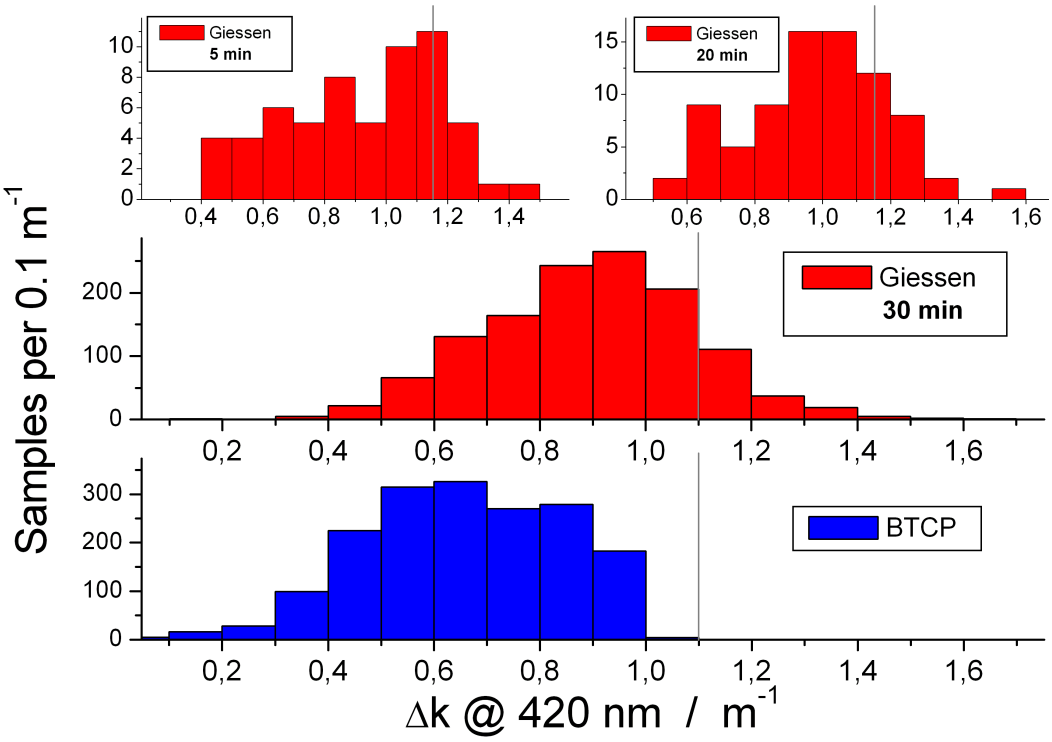

Figure 4.8: Δk measurements from BTCP and Gießen.

Conclusion concerning the radiation hardness:
201 crystals have to be rejected.

4.3 Correlations between measurements of BTCP, CERN and Gießen

Due to two in principle absolutely similar devices at BTCP and CERN one would expect clear and explicit correlations between the data of both facilities. This is not the typical case because of different conditions which were not specified in the contract in detail. In comparison to the transmission and Δk data measured in Gießen, one would expect correlations but also constant shifts due to the completely different ways of measuring (explained in 3.2.1.1 and 3.2.1.2). Furthermore, the correlation coefficient (CC) which is defined for a set of two variables X and Y as

$$\mathrm{CC} \;=\; \frac{<((X-<X>)\cdot(Y-<Y>))>}{\sigma_X \cdot \sigma_Y} \in [-1;+1]$$

gives an additional statement if a correlation exist.
As an example for the transmission, Fig 4.9 shows a correlation between BTCP and CERN distinguished by the geometry at 420 nm of the first lot. The color code on the right side of each histogram stands for the amount of data points in a certain region. In case of the barrel type crystals the data appear to be correlated with a CC of 0.6. But in spite of the similar concept, no correlation becomes visible for the EC geometry (CC$\approx$ 0). The geometry depending correlation could be linked to the spread of the testing beam which is not known. This fact would also explain the more pronounced systematic shift for the barrel crystals by a comparison of BTCP and CERN data in Fig. 4.11 in contrast to a confirmed correlation with the result from Gießne in case of the transmission at 420 nm.
Another slightly conspicuous aspect is that the values from Gießen are more broadly distributed than for the others. But this is a general fact and can also be verified by looking at Fig. 4.5. One negligible contribution to that broadening is the sensibility of a more focused test beam on the orientation of the optical axis which is usually parallel to the long crystal axis, but it can vary by a few degrees. Calculations with a deviation of 5° result in an error on the per mille level for the transmission.
Nevertheless, all measurements confirm the excellent optical quality, since all crystals provide a transmission well above the required limits.

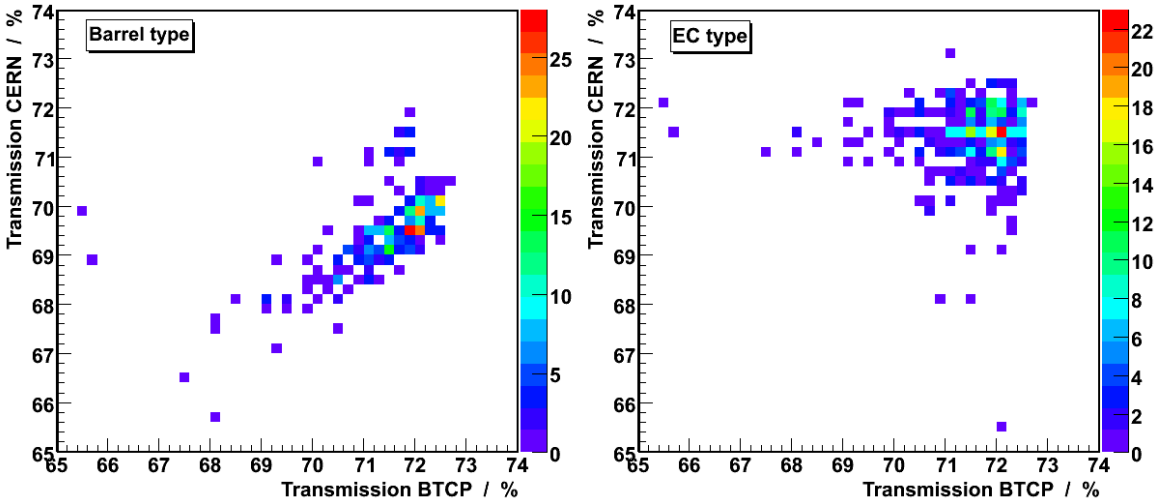

Figure 4.9: Correlation concerning the transmission at 420 nm for the first two lots between BTCP and CERN. Left: Barrel Type. Right: EC Type.

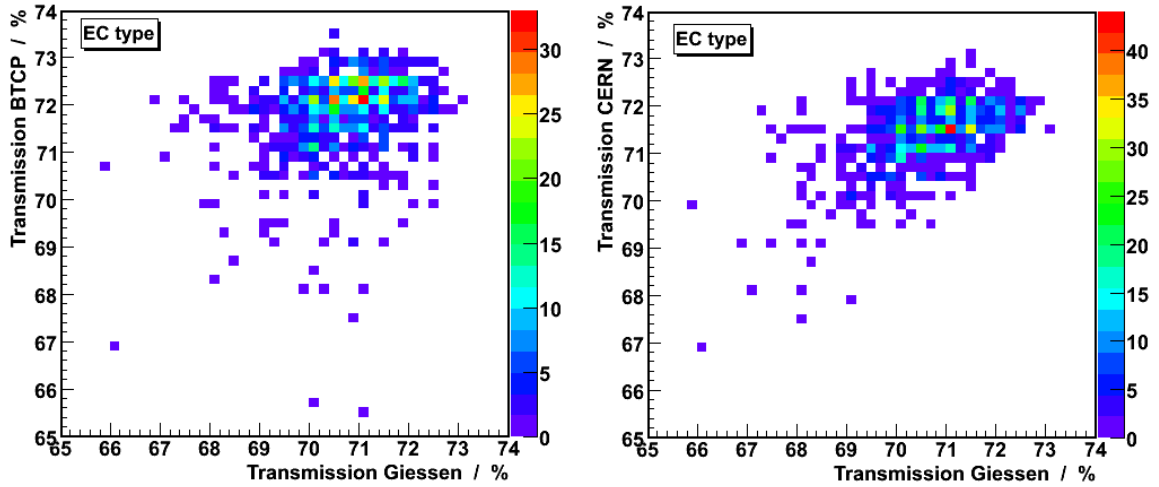

Figure 4.10: Correlation of EC crystals for the transmission at 420 nm of the first two lots. Left: BTCP-Gießen. Right: CERN-Gießen.

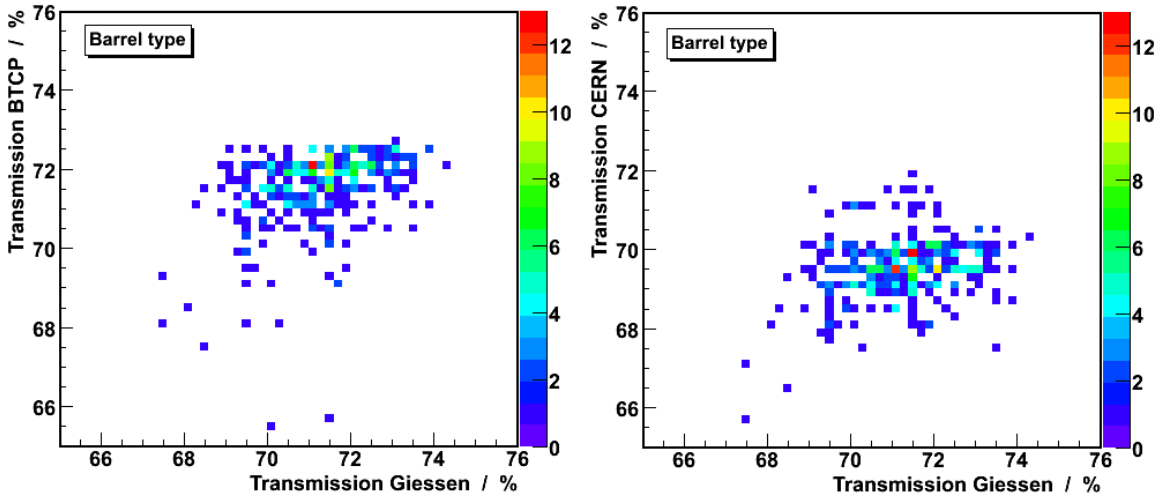

Figure 4.11: Correlation of barrel crystals for the transmission at 420 nm of the first two lots. The upper picture shows EC, the lower one barrel type crystals.

Further correlations are not really understandable mainly due to not provided measurement protocols and procedures, e.g. the correlation between the $\Delta\lambda$ from BTCP and CERN for barrel crystals (Fig 4.12, left) which shows a difference by a factor of 2. For the EC crystals, the values are comparable but they are also randomly distributed (Fig 4.12, right) which is reflected in the CC, too. This probably originates from different beam shapes, since the mechanical arrangement should be similar and other conditions should not have a significant impact. This discrepancy is, however, acceptable because all crystals are far below the limit of 3 nm.
Another relation, that is not understandable, is the correlation of LY data for lot 1 shown in Fig. 4.13 distinguished by geometry. In case of the barrel crystals no correlation becomes visible. Especially the large absolute shift can not be explained. The normalization factor, which depends on the geometry, is not known and therefore the originally measured data in arbitrary units from the ACCOS machine at BTCP is not reproducible.

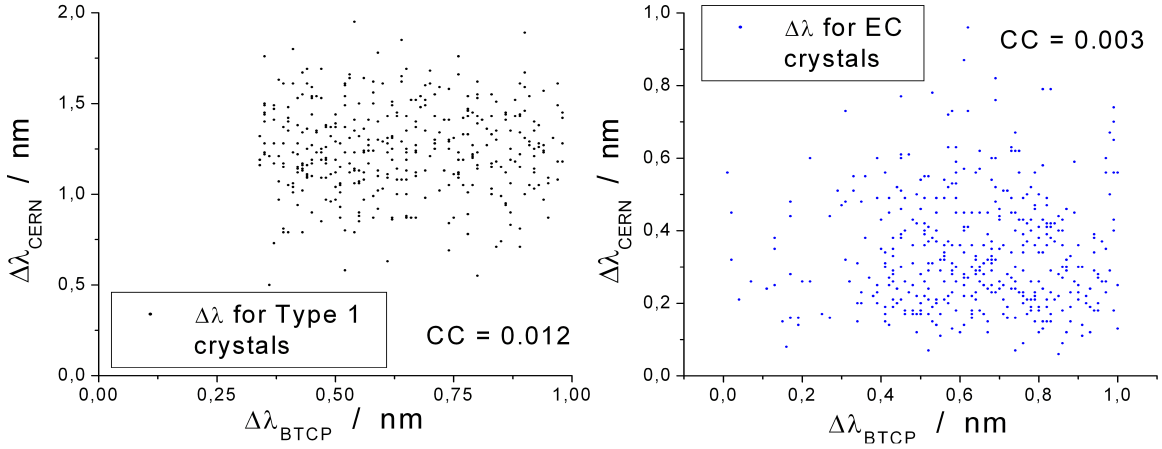

Figure 4.12: Correlation $\Delta\lambda$ for BTCP and CERN. Left: Type 1 crystals. Right: EC crystals.

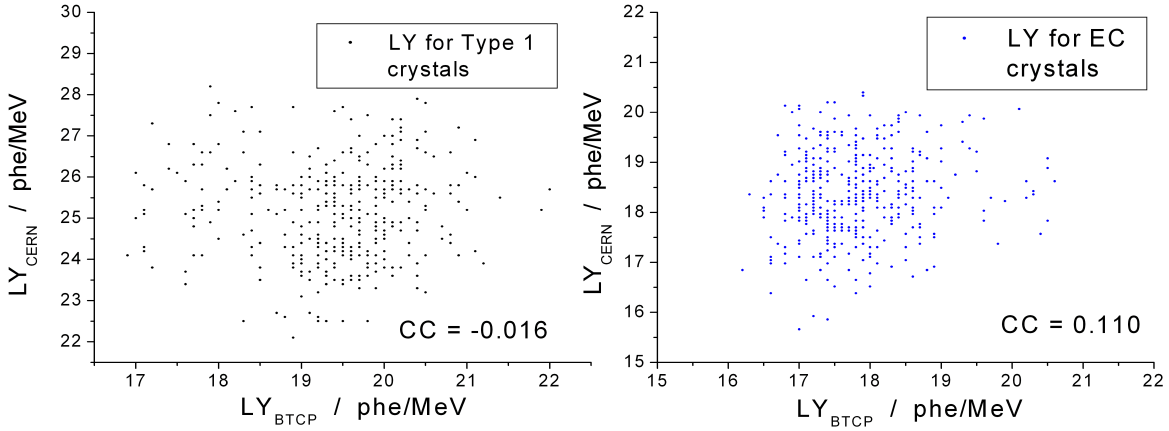

Figure 4.13: Correlation LY for BTCP and CERN. Left: Type 1 crystals. Right: EC crystals.

One important correlation concerning the Δk data was already shown in the previous chapter (Fig. 3.26) for the EC crystals of lot 1 and 2. This correlation looks reasonable and the same is true for the majority of barrel crystals in Fig. 4.14 which is indicated by the linear regression of the EC crystals marked as black line. In Fig. 4.14 one can also find an additional distribution marked with a red ellipse. The origin of this amount of points ($\sim$ 60 crystals) is unknown but probably due to a temporary systematic error at one of both facilities. It is possible that the initial starting measurements at Gießen were influenced by a not well adjusted spectrometer. This can be verified by remeasuring that group of crystals which has not been performed yet.
Concluding the discussion of figures 3.26 and 4.14, the systematic shift and slope of the results strongly depend on the crystal geometry, the temperature of the environment and the time, when the measurement was performed after the end of irradiation. The contract only defines an overall dose of 30 Gy and a temperature of T=(20 ± 5)°C.

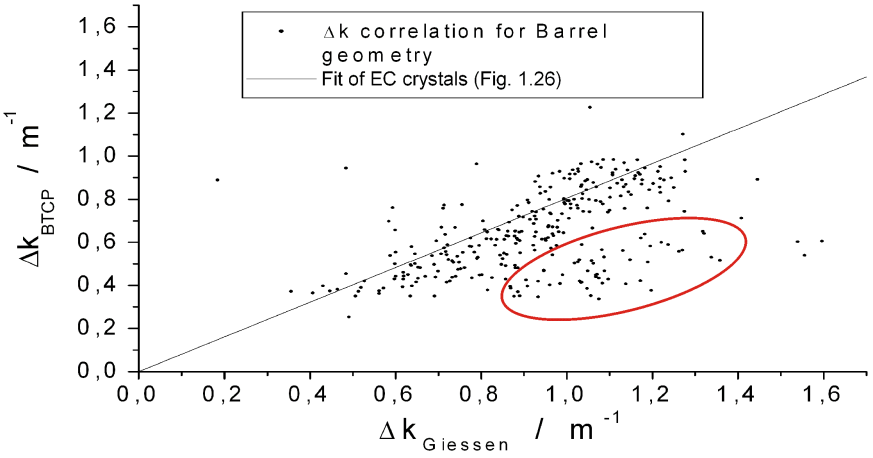

Figure 4.14: Correlation Δk of BTCP and Gießen for Barrel crystals. The point of interest is the encircled area which shows an additional distribution.

4.4 Results with respect to CMS specifications

The CMS detector, with a weight of roughly 12500 tons was started in 2000 to be installed at the LHC at CERN. CMS will be mainly used in the search for Higgs bosons and new particles (e.g. supersymmetric particles). The whole ECAL contains almost 80000 lead tungstate crystals to allow among others the observation of $H \rightarrow \gamma\gamma$ decays with a low signal-to-background ratio due to an irreducible background.
The initial conditions for the ECAL of CMS were different with respect to $\overline{\text{P}}$ANDA. Tab. 4.2 shows the main differences of the two generations of lead tungstate and the expected requirements of the calorimeters.

	Unit	PWO I CMS	PWO II $\overline{\text{P}}$ANDA
liminescence maximum	nm	420	420
Lanthanum and Yttrium concentration level	ppm	100	40
LY at room temperature	phe/MeV	$8-12$	$17-22$
expected energy range of EMC	GeV	$0.15-1000$	$0.01-10$
EMC operating temperature	°C	+18	-25
energy resolution of EMC at 1 GeV	%	3.4	2.0

Table 4.2: Comparison between CMS and $\overline{\text{P}}$ANDA concerning the different generations of lead tungstate and the desired applications.

The geometrical tolerances and required surface quality of CMS crystals are quite similar compared to the specifications for $\overline{\text{P}}$ANDA introduced in 3.1. Differences between the defined values and the edges of the produced quantities in the range of $0/-0.1$ mm are allowed. Also the roughness of the surfaces should be guaranteed with an accuracy less than 0.02 μm.
In case of the LY it was desired to have more than 8 phe/MeV with an additional condition that the radioactive source is located at 8 X_0 from the small end of the crystal. This position corresponds to the shower maximum for an incoming photon or electron with $50-100$ GeV. In addition to avoid degrading the constant term of the energy resolution due to longitudinal shower fluctuations, the LY has to remain constant along the long axis between 3 X_0 and 15 X_0 distance from the crystal front face. This condition is expressed in the FNUF[5] with

$$-0.35\%/X_0 \leq \quad \text{FNUF} \quad \leq +0.35\%/X_0$$

[5]FNUF = Front Non-Uniformity Factor

This is achieved by roughing the lateral crystal surfaces with a well defined roughness. The latter condition was not specified for the $\overline{\text{P}}$ANDA crystals but for the overall LY one can conclude that the further development of lead tungstate leads to an improvement of the factor of 2 and therefore the specification limit of $\leq$ 16 phe/MeV was successfully achieved.
For the optical properties CMS required the following limits:

	Unit	Limit
transmission @ 360 nm	%	25
transmission @ 420 nm	%	55
transmission @ 620 nm	%	65
transversal transmission dispersion $\Delta\lambda$	nm	3

Table 4.3: Optical specifications for the CMS crystals. The required value for the $\Delta\lambda$ is the same with respect to $\overline{\text{P}}$ANDA but in the meantime the longitudinal specifications were increased.

The specification for the transverse uniformity which is expressed by $\Delta\lambda$ did not change, but one can point out that this property is slightly improved. After the analysis of the first two lots, the mean values is about 0.57 nm (CMS analysed 27000 crystals: $<\Delta\lambda> = 0.62$ nm). Also the longitudinal transmission shows a significant improvement which causes an enhancement on the specifications limits. For 360 nm the enhancement is even twice as much (10% more) with respect to 420 nm and 620 nm which is an indication for less defects in a crystal. All these facts are due to the successful realization of technological improvements of manufacturing.
In case of the radiation hardness Fig. 4.15 shows a Δk distribution for a random production run of CMS crystals. One can clearly see that the mean value is shifted to the right with respect to the preliminary $\overline{\text{P}}$ANDA data but one also has to keep in mind the different conditions concerning the dose. That is the reason why the shifting is more pronounced. To be able to compare the radiation hardness one has to normalize the mean values for CMS and $\overline{\text{P}}$ANDA, that means Fig. 4.15 and 4.8 respectively. For $\overline{\text{P}}$ANDA we reach a saturation level of approximately 80% with 30 Gy (compare Fig. 2.3). To get a rough estimation of the difference according radiation hardness, one can express the mentioned numbers ($<\Delta\text{k}>_{\overline{\text{P}}\text{ANDA}}$ from Gießen) in the relations:

$$\begin{aligned} <\Delta\text{k}>_{\overline{\text{P}}\text{ANDA}} &= 0.89\ \text{m}^{-1} \\ <\Delta\text{k}>_{\text{CMS}} \cdot 80\% &= 1.23\ \text{m}^{-1} \cdot 80\% = 0.98\ \text{m}^{-1} \\ \Rightarrow <\Delta\text{k}>_{\overline{\text{P}}\text{ANDA}} &< <\Delta\text{k}>_{\text{CMS}} \cdot 80\% \end{aligned}$$

The conclusion is that the radiation hardness was significantly improved.

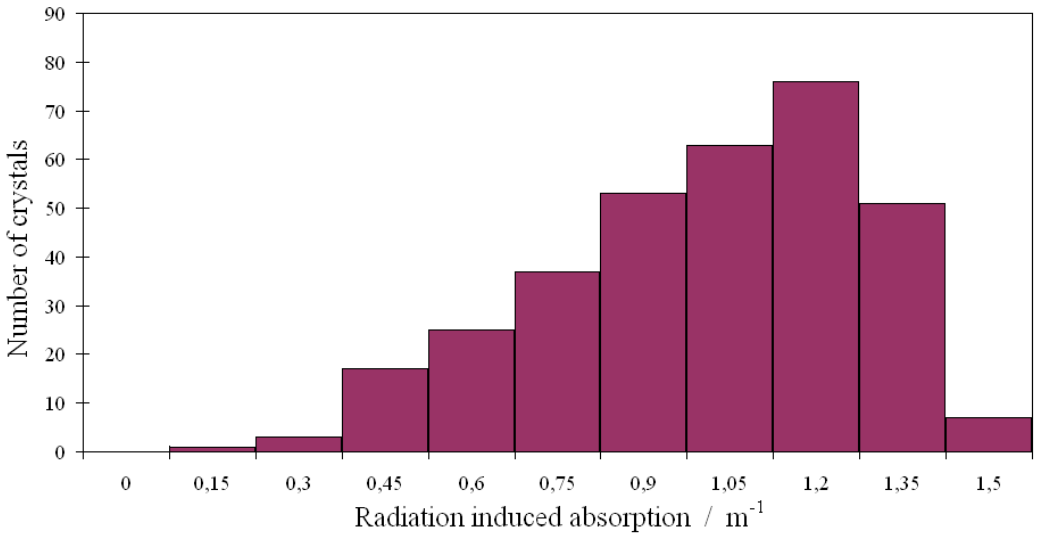

Figure 4.15: Δk distribution of several random CMS crystals for one production run [VD]. The Gaussian-like spectrum (mean value of 1.23 m^{-1}) is cut at the specification limit of 1.5 m^{-1}.

Chapter 5

Discussion and Outlook

This chapter is intended as a summary on the first results of mass production of the lead tungstate crystals for the $\overline{\text{P}}$ANDA EMC. Some crucial effects and error estimations will be discussed with respect to the simulations performed with LITRANI. At the end an overview over the present delivery status and an outlook on further inspections is given

5.1 Review of the inspection and achieved quality

In first approximation besides the radiation hardness nearly all crystals fulfill the aimed specification limits. Due to the optimized procedure of manufacturing the quality parameters fit by within narrow distributions. As characteristic for this investigation one can point out that the quality control is performed in much more detail compared to CMS. In case of CMS only randomly selected tests were possible because of the huge amount of crystals, but for $\overline{\text{P}}$ANDA each crystal is tested for its individual properties. Furthermore the final evaluation of the inspection is independent of the quality parameters obtained from BTCP. Comparisons between the values from BTCP, CERN and Gießen show a mixture of good correlations and discrepancies. Even in spite of the similar devices which are used for the test procedures at BTCP and CERN clear correlations of the measured values can not be observed in all cases, as discussed in Sec. 4.3. These disagreements have to be recognized but can not be further investigated or explained because of a lack of detailed measurement reports and partly because of not precisely enough defined conditions of the measurement methods.
There is no necessity for rejection of crystals because of the geometry, longitudinal transmission and the homogeneity along the crystal axis. Especially the two latter ones are well within the specification limits. In case of the LY probably only EC type crystals have to be considered for rejection due to their closeness to the specification

limit at 16 phe/MeV. As it was mentioned, the stronger tapered crystals show a significantly higher LY because of the more efficient focusing effect. This fact was again confirmed by the simulations in Sec. 3.3.3, the result obtained in Fig. 3.18 and the calculations in Sec. 4.2.4.
The most crucial parameter is the radiation hardness expressed as change Δk of the absorption coefficient. The final check is done at Gießen with an optimized light beam which was realized by an additional set up consisting of lenses and mirrors by the HUND company. Due to the small diameter of the beam and the planarity of the end faces of each crystal geometry, one can expect to be completely geometry independent and to have negligible reflections on the side surfaces. Several error contributions were taken into account to estimate a more appropriate and acceptable upper limit for the radiation hardness of $\Delta k = 1.1\ m^{-1}$ for crystals which were remeasured 30 minutes after irradiation. The size of the error contribution due to multiply reflected photons was confirmed by simulations in a nearly identical setup. The obtained results (Fig. 3.11) and subsequently calculated error agree with the theoretical prediction. Considering the modified specification limit, roughly 11% of the here reported lots have to be rejected due their insufficient radiation hardness.
The achieved quality of the crystals which were analyzed in this thesis shows a clear improvement in almost all parameters in comparison to PWO I. Especially the enhancement of radiation hardness and light yield open up the possibility for PWO II to be considered for upgrades of existing electromagnetic calorimeters (like e.g. Belle[1], LHCb or even CMS) or to be exploited in future experiments.
Another interesting effect which accidentally came up during the first Δk-measurements, was the recovery by illumination with near infrared light. A first investigation of this option of "online-recovery" is shown in Fig. 5.1.

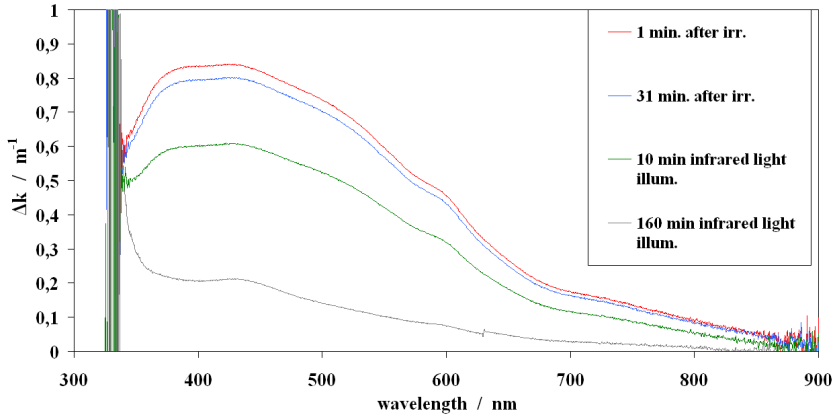

Figure 5.1: First investigations of recovery by illumination with infrared light (λ = 940 nm) [VD]. This patented effect is an option to perform "online-recovery" during the beam time.

[1] experiment at the KEK B-factory in Japan with the primary goal to study the origin of CP violation

5.2 Non-linearity of light collection efficiency

Fig. 3.18 documents the large difference of the position dependence of the light collection efficiency along the main crystal axis for the maximum and minimum tapered crystals (Type 1 and EC). This figure shows the non-linearity of the light collection depending on the distance between the sensor and the place of origin of the scintillation light. This effect is almost negligible for EC crystals and originates from an interplay between focusing and absorption as illustrated in Fig. 5.2. The non-linearity of the

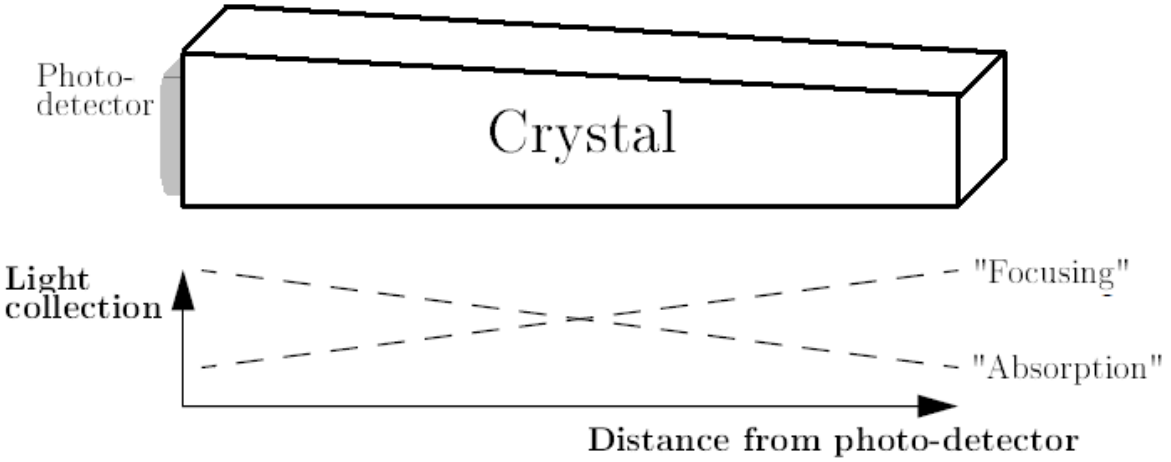

Figure 5.2: Schematic illustration of the interplay between focusing and absorption in a tapered crystal [CMS8].

light yield collection is tolerable in the first third of the crystal with respect to the small end face and with a sufficiently low incoming energy which is comparable to the expected photon energy of $\overline{\text{P}}$ANDA. Only at significant higher energies the non-linearity will affect the energy response. One way to avoid this effect is to rough up the crystal surfaces similar to CMS or to reduce the reflectivity of the cover. In both cases a loss of light has to be taken into account due to the more diffuse reflections or even total absorption. This is the reason why this possibility is no adequate solution for the $\overline{\text{P}}$ANDA detector due to the importance of LY.

5.3 Outlook for the further lots

Within this thesis the first two lots containing 1750 crystals were completely analyzed. They correspond to approximately 11% of the hole EMC. In the meantime altogether nine lots were produced and the majority already arrived at Gießen. Tab. 5.1 gives a short overview about the present production status and the geometry types produced so far. Presently it is not quite sure whether BTCP will continue with the production

Type		Lot B1 - B4	Lot B5	Lot B6	Lot B7	Lot B8	Lot B9
FEC		4400		—	—	—	—
BEC		—	—	—	—	70	630
Barrel	Type 1	375	—	270	695	—	—
	Type 2	—	—	—	—	140	—
	Type 9	—	—	330	325	—	—
	Type 10	—	—	—	—	120	—
Total		4775		600	1020	330	630

Table 5.1: Present delivery status of the lead tungstate crystals. Altogether 7355 crystals are produced which correspond to roughly 45% of the EMC. The majority is presently stored in Gießen and only a small fraction of lot 5 and 6 is under investigation at CERN.

of the remaining lead tungstate crystals. An alternative producer could be SICCAS[2] in Shanghai.
Another crucial point is the reproducibility and stability of the crystal properties. The complete analysis was finished for the first two lots, but for these lots and a few more one can make a preliminary statement concerning those properties which were only deduced at BTCP and CERN, e.g. the homogeneity ($\Delta\lambda$) and the LY. Fig. 5.3 shows the obtained $\Delta\lambda$- and LY-values from CERN for the first four lots.
As it was mentioned, the required quality is not expected to become a problem due to the stringent specifications in the contract. But in addition, as identical in Fig. 5.3 even the mean values of the performance parameters stay nearly constant. This holds also for the longitudinal transmission at the relevant wavelengths which is expressed by the mean values given in Tab. 5.2. In case of the LY there is no significant change of the distributions for EC crystals. The EC crystals represent the largest amount of a particular geometry of the hole EMC ($\sim$ 28%). Therefore one can expect that

[2]SICCAS = Shanghai Institute of Ceramics, Chinese Academy of Sciences

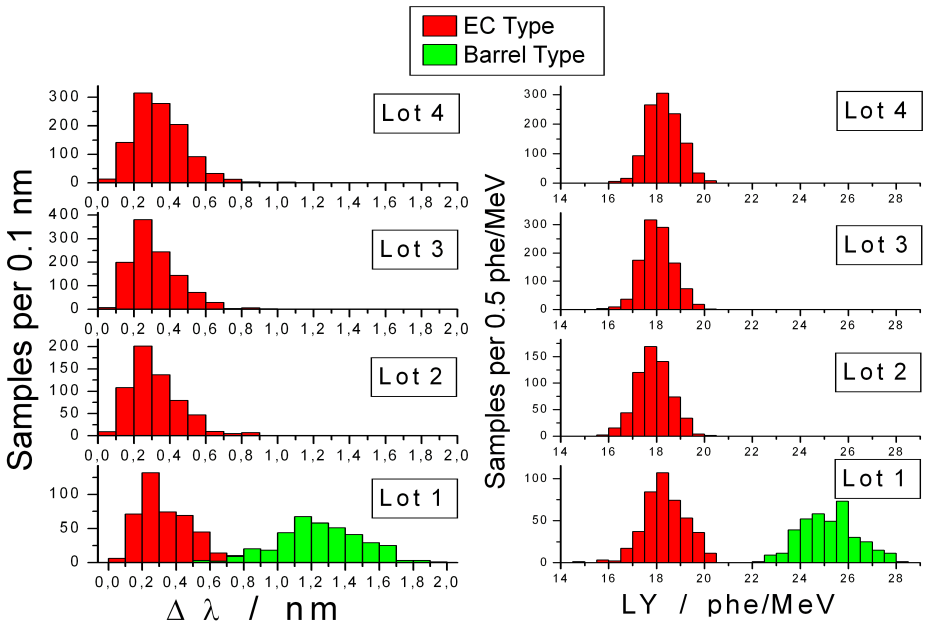

Figure 5.3: Distributions of $\Delta\lambda$- and LY-values from CERN for the first four lots distinguished by the geometry.

the remaining geometries can be produced with the same continuity in quality. As a positive consequence the $\overline{\text{P}}$ANDA EMC will be nearly independent in φ-direction since the segmentation along the circumference is realized with crystals of identical geometry. On the other hand the unavoidable ϑ-dependence due to the different geometries in one slice (e.g for the LY) has to be calibrated subsequently.

Lot	Mean Value in % for			St. Deviation in % for		
	T(360 nm)	T(420 nm)	T(620 nm)	T(360 nm)	T(420 nm)	T(620 nm)
B-1	51.35	71.34	75.41	1.67	0.67	0.34
B-2	51.62	71.45	75.43	1.25	0.62	0.36
B-3	50.93	71.58	75.43	1.29	0.57	0.34
B-4	51.35	71.86	75.55	1.21	0.62	0.34

Table 5.2: Fit parameters of the longitudinal transmission for the first four lots from CERN at the three relevant wavelengths. Only EC crystals were taken into account to avoid any effect which depends on the geometry.

List of Figures

List of Tables

Bibliography

[AA] A. Annenkov *Improved light yield of lead tungstate scintillators*, 2000

[ACC] E. Auffray *Performance of ACCOS, an Automatic Crystal quality Control System for the PWO crystals of the CMS calorimeter*, 2001

[ACC1] *Studies and Proposals for an Automatic Crystal Control System*

[BAC] S. Baccaro et al. *Ordinary and extraordinary complex refractive index of the lead tungstate ($PbWO_4$) crystal*, 1997

[CMS] http://cms.web.cern.ch/cms/index.html

[CMS1] CMS Note: *Correlation between Light Yield and Longitudinal Transmission in PWO crystals and impact on the precision of the crystal intercalibration.* May 2004

[CMS2] CMS Physics TDR Vol. 1: http://cdsweb.cern.ch/record/922757/files/lhcc-2006-001.pdf, 2006

[CMS3] J.P. Ernenwein, CMS Conference Report *Overview of the CMS electromagnetic calorimeter*

[CMS4] E. Auffray *Overview of the properties of PWO crystals for the CMS electromagnetic calorimeter at CERN*

[CMS5] CMS Note: *Concurrent Repository & Information System for Tracking Assembly and production Lifecycles*, 1996

[CMS6] CMS Note: *Cross-calibration of two automatic quality control systems for the CMS ECAL crystals*, 2004

[CMS7] CMS Note: *Studies and Proposals for an Automatic Crystal Control System*, 1997

[CMS8] CMS Note: *Development of a Uniformisation Procedure for the $PbW0_4$ Crystals of the CMS Electromagnetic Calorimeter*

[COMP] F. Arqueros and G. D. Montesinos *A simple algorithm for the transport of gamma rays in a medium*, January 2003

[DBCS] Photon Cross Sections Database: http://physics.nist.gov/PhysRefData/Xcom/Text/XCOM.html

[HAM] http://sales.hamamatsu.com/en/products/electron-tube-division/detectors/photomultiplier-tubes/part-r2059.php#

[HUN] provided by the HUND Company, http://www.hund.de/

[KIN] http://pcweb.physik.uni-giessen.de/panda/publications/reports/status20report202003200523.pdf

[LIT1] F.X. Gentit *Litrani: a general purpose Monte-Carlo program simulating light propagation in isotropic or anisotropic media*

[LIT2] http://gentit.home.cern.ch/gentit/litrani/

[MAMO] M. Moritz, Diploma Thesis "Ansprechverhalten des PROTO 60, Untereinheit des PANDA-Detektors, auf hochenergetische Photonen", 2009

[MM] M. Marteinsdottir, Talk, PANDA Collaboration Meeting GSI, March 2009 http://www-panda.gsi.de/db/meetingDBr/emc/090303/MM17-090303_Maria_linearity.ppt

[MySQL] http://www.mysql.com

[POH] R.W. Pohl *Optik und Atomphysik*, 11. Auflage Springer-Verlag

[NOV1] R. Novotny, Lecture: *Messmethoden der Kern- und Teilchenphysik*

[NOV2] R. Novotny, *Radiation Hardness and Recovery Processes of Cooled PWO-II Crystals for PANDA*, 2008

[PPR] PANDA-Collaboration *Physics Performance Report for PANDA*, March 2009

[TDR] PANDA-Collaboration *Technical Design Report for the EMC of PANDA*, October 2008

[TPR] PANDA-Collaboration *Technical Progress Report for PANDA*, February 2005

[VAR] http://www.varianinc.com/image/vimage/docs/products/spectr/uv/brochure/1942.pdf

[VD] provided by V. Dormenev (II. Physical Institute, JLU Giessen)

[VM] V. Metag, Group Lecture 2008

Index

Appendix A

Fit Parameters

Property	*Condition*	*Facility*	*Geometry*	*Unit*	*Mean Value*	*St. Deviation*
Geometry: Deviation of	Dim L	BTCP	all	mm	0.038	0.034
	Dim AF				0.047	0.015
	Dim BF3				0.048	0.014
	Dim BF4				0.051	0.015
	Dim CF				0.045	0.015
	Dim AR				0.042	0.016
	Dim BR3				0.039	0.015
	Dim BR4				0.043	0.014
	Dim CR				0.041	0.015
	Dim L	CERN	all	mm	0.030	0.034
	Dim AF				0.064	0.015
	Dim BF3				0.040	0.014
	Dim BF4				0.042	0.015
	Dim CF				0.063	0.016
	Dim AR				0.052	0.016
	Dim BR3				0.033	0.015
	Dim BR4				0.036	0.014
	Dim CR				0.052	0.016

Longitudinal Transmission	at 360 nm	BTCP	all	%	50.374	1.368
	at 420 nm				72.000	0.870
	at 620 nm				76.055	0.608
	at 360 nm	CERN	all	%	50.885	1.809
	at 420 nm				70.919	1.079
	at 620 nm				75.093	0.657
	at 360 nm	Gießen	all	%	49.590	1.822
	at 420 nm				70.815	1.138
	at 620 nm				76.870	1.076
Non-Uniformity $\Delta\lambda$		BTCP	EC Type 1	nm	0.555	0.219
					0.533	0.225
		CERN	EC Type 1	nm	0.555	0.219
					1.246	0.244
Light Yield	T= +18°C	BTCP	EC Type 1	phe/MeV	18.040	0.775
					19.398	0.900
	T= +18°C	CERN	EC Type 1		18.109	0.773
					25.015	1.156
Radiation Hardness Δk		BTCP	all	m^{-1}	0.654	0.187
	Delay:	Gießen	all	m^{-1}		
	5 min				0.917	0.249
	20 min				0.979	0.205
	30 min				0.890	0.199

Table A.1: Fit parameters for the analyzed crystals of lot 1 and 2.

Hiermit versichere ich, dass diese Arbeit ohne Hilfe Dritter und ohne Benutzung anderer als den angegebenen Quellen und Hilfsmittel angefertigt wurde.
Diese Arbeit wurde in gleicher oder ähnlicher Form noch keiner Prüfungsbehörde vorgelegt.

Tobias Eißner
Gießen, im August 2009